The influence of grain crushing and pore collapse on the formation of faults

N.A. Collins-Craft[1,†], I. Stefanou[2,⋆], J. Sulem[1], and I. Einav[3]

[1]Laboratoire Navier, École Nationale des Ponts et Chaussées, Institut Polytechnique de Paris, Université Gustave Eiffel, CNRS, Champs-sur-Marne, France
[2]IMSIA (UMR 9219), CNRS, EDF, CEA, ENSTA Paris, Institut Polytechnique de Paris, Palaiseau, France
[3]Particles and Grains Laboratory, The School of Civil Engineering, The University of Sydney, Sydney, Australia
[†]Previously at Univ. Grenoble Alpes, Inria, CNRS, Grenoble INP, LJK, 38000, Grenoble, France
[⋆]Previously at GeM (Institute de Recherche en Genie Civile et Mécanique), École Centrale de Nantes, Université de Nantes, CNRS, Nantes, France

27th December 2025

Key points

- A new model accounts for the coevolution of the grain size distribution and porosity in crushable granular media subject to shearing.
- Linear stability analysis and the finite element method are used to study the localisation width of the model at depth.
- Orders-of-magnitude decrease in permeability is predicted to occur inside the fault core, but permeability can increase outside it.

Abstract

During an earthquake, slip occurs in a localised shear zone that features a heavily granulated fault core that can be characterised as a shear band. We study the formation of this fault core in a granular rock such as sandstone by developing a model of crushable granular media within the framework of Breakage Mechanics. This model accounts for the evolution of the grain size distribution, while also accounting for the co-evolution of the solid fraction. An enrichment with the Cosserat continuum allows for the model to predict finite-width shear bands. The model is then calibrated against experimental data taken from tests on Bentheim sandstone, and a parametric study of the mechanical parameters is conducted using linear stability analysis. We find that for deeply-buried rocks the shear bands have a compactive component, and the initial value of the solid fraction does not play a strong role in the initial band thickness, but can influence the rate of delocalisation of the band. Post-localisation behaviour is studied with the finite element method, which shows the formation of zones of dilation outside the band in addition to the compaction within the band. Using a modified Kozeny–Carman permeability law, it is shown that within the band the permeability reduces by several orders of magnitude, but can increase outside the band. Our results highlight the importance of modelling grain size and solid fraction evolution as they exert a controlling influence on hydromechanical properties that play an important role in fault formation and seismic slip.

Plain language summary

During an earthquake, all of the sliding motion is accommodated in a very narrow zone. Within this zone, the material has much finer grains than in the surrounding rock. To understand how this arises we develop a new model that tracks how the grains become finer, as well as how the porosity of the material reduces. The model can predict how wide the narrow zone of fine material is. We show that during the sliding process, strain localises in a narrow compacting shear band where significant grain crushing is accompanied by porosity reduction whereas porosity increase occurs outside the band. These changes in porosity and grain size strongly impact the permeability of the medium, reducing it by orders of magnitude in the compacting slip zone. This process is very important as materials through which it is difficult for fluids to flow are known to be more prone to earthquakes.

Keywords

Breakage; Solid fraction; Shear bands; Cosserat continuum; Bentheim sandstone; Permeability changes

1 Introduction

Failure due to localisation into a shear band is particularly important in soils and rocks, as this failure mode is what governs the formation of a (potentially seismogenic) fault (Barras and Brantut, 2025). While the faulting process can occur in completely dry soils and rocks in both the field (Aydin and Johnson, 1978, 1983) and laboratory (Ord et al., 1991), shear band formation can also be influenced by changes to pore fluid pressure, flash melting and phase changes (Rice, 2006; Veveakis et al., 2010; Brantut et al., 2011; Brantut and Sulem, 2012; Veveakis et al., 2013; Platt et al., 2014; Rice et al., 2014; Platt et al., 2015). These processes are known to co-evolve as the fault forms and matures, with the structural consequence of the localisation of deformation into a thin band, that is typically referred to as the principal slip zone (PSZ) of the fault. The PSZ accommodates the majority of slip in a fault (Chester and Chester, 1998; Sibson, 2003; Wibberley and Shimamoto, 2003; Sulem, 2007), and the intensity of the multiphysical processes governing the fault behaviour is controlled by the thickness of the PSZ (Brantut et al., 2011; Veveakis et al., 2013; Platt et al., 2015; Sulem and Stefanou, 2016), meaning that an accurate prediction of the evolution of this thickness is essential to accurately model fault behaviour.

Within the PSZ, the grain size distribution (GSD) features a considerably higher proportion of fine grains than the surrounding host rocks and generally follows a power-law scaling in mature faults (Sammis et al., 1986, 1987; Sammis and Biegel, 1989; An and Sammis, 1994). The role of this microstructural property and its evolution in fault formation and behaviour has to this point been comparatively minimally studied. Aside from any effect that changes to the GSD can have on the mechanical behaviour in and of itself, any change to the GSD will also change the coupled multiphysical phenomena within the fault. As the GSD changes due to comminution, the surface area of the solid material will increase, which will in turn increase the rate of any chemical interactions that occur between the solid and the pore fluid (Stefanou and Sulem, 2014; Buscarnera and Das, 2016; Zhang and Buscarnera, 2018; Viswanath and Das, 2019; Chen et al., 2023; Chen and Einav, 2024). The evolution of the solid skeleton towards a more efficient packing will reduce the available space for the pore fluid to occupy. Simultaneously, the movement from larger to smaller pores defined by much smaller and more tightly packed grains leads to the tortuosity of the system also increasing, and as a consequence the permeability decreasing (Manzocchi et al., 1998; Haines et al., 2016). The process of shearing, and the associated frictional sliding and grain breakage will also increase the temperature, further increasing the pore pressure (Rattez, 2017; Rattez et al., 2018a,b,c; Stathas and Stefanou, 2023) and possibly modifying the rate of any chemical reactions. All of these phenomena are tightly coupled, serving to change the effective stress experienced by the solid skeleton, which will in turn change the mechanical state by facilitating further shear deformation. This deformation leads to further changes in the GSD. This highlights the importance of being able to accurately model the evolution of the grains in the solid skeleton in order to fully capture the multiphysical behaviours that influence fault formation.

Even in cases of shallow burial depth and slow deformation (meaning thermal and chemical effects do not play any significant role), cataclastic shear band formation with significant grain breakage and porosity change is observed in the field (Aydin and Johnson, 1978, 1983; Cashman and Cashman, 2000; Fossen et al., 2007; Exner and Tschegg, 2012; Lommatzsch et al., 2015; Pizzati et al., 2020). These bands can also be observed in laboratory experiments performed in a wide variety of apparatuses (Bésuelle et al., 2000; Chambon et al., 2002; Desrues and Viggiani, 2004; Sulem and Ouffroukh, 2006), including in tests that are conducted without any pore fluid (Rattez et al., 2022). We may conclude that shear band formation is a pervasive feature of deforming granular rocks and soils, regardless of the presence of multiphysical couplings. This fact was demonstrated theoretically in the classic paper of Rudnicki and Rice (1975) by studying the bifurcation behaviour of a general class of constitutive models appropriate for frictional materials such as soil and rocks. It has further been shown that in the classical continuum with rate-independent plasticity the favoured localisation mode is a band of infinitely small thickness (Stefanou and Alevizos, 2016). In numerical simulations such as those performed with the finite element method (FEM) this will result in a band of one element width, regardless of the mesh refinement.

The ultimate reason for this infinitely thin localisation is the absence of an internal length scale in the material model (Mühlhaus, 1986; Mühlhaus and Vardoulakis, 1987), a problem solved by specifying a model that does have such a length scale. This can be achieved by working with a model that includes viscosity, as this quantity introduces a dimension of length (de Borst and Duretz, 2020). However, recent results have demonstrated that for rate-dependent regularisation, strain localisation onto a plane remains theoretically possible and has been observed numerically (Stathas and Stefanou, 2022). In particular, whether the localisation onto a plane occurs in a given simulation is determined by the length of time simulated relative to the characteristic time introduced by the viscosity. We would prefer that the ability of a model to regularise localisation not be dependent on arbitrary simulation choices

such as the cut-off time, but instead on the underlying physics of the system. Hence, while viscous systems may better reflect the observed rate-dependence of real materials, viscosity appears inadequate to reliably regularise the localisation of the system. Another possible method of regularisation is to include additional physics such as thermal, hydrological and chemical interactions. In this case, the internal length scale is linked to diffusion processes (see Rice (2006), Brantut et al. (2017), Jacquey et al. (2021) and Heimisson et al. (2022)), particularly the outwards diffusion of pore pressure and temperature from the shear band into the bulk, as well as possibly the movement of chemical species. However, Gerolymatou et al. (2024) have recently shown that for mechanical systems coupled with physics described by an advection-diffusion equation (namely pore fluid diffusion, thermal diffusion and chemical species diffusion, as well as mechanical quantities such as the "granular entropy" (Jiang and Liu, 2009)), the presence of these processes is not necessarily sufficient to guarantee regularisation. In particular, if the diffusivity depends on the strain (as permeability can), regularisation will not occur. If the advection-diffusion source term depends on the strain rate (as temperature or granular entropy do), regularisation depends on the system parameters which may change as the system evolves, making *a priori* conclusions impossible. For some physical processes (*e.g.* shear heating induced by friction), the parameter values will necessarily be those that do not regularise the system. As such, we can infer that multiphysical couplings are not able to *a priori* regularise mechanical systems. Further, localisation in dry granular materials at room temperature is widely observed experimentally (see for instance Charalampidou et al. (2011) and Karatza et al. (2018)), meaning that a purely mechanical model without multiphysical couplings is required to explain these observations, although there remains considerable interest in including hydrological, thermal and chemical effects in general models of faults (Rattez et al., 2018a,c) to obtain a more refined description of their behaviour. The third approach to regularisation is *via* a continuum with microstructure such as a nonlocal continuum (Pijaudier-Cabot and Bažant, 1988; Poh and Sun, 2017; Wang and Poh, 2018), the second gradient continuum (Zervos et al., 2001) or the Cosserat continuum (Cosserat and Cosserat, 1909; Mühlhaus and Vardoulakis, 1987), where the length scale is an inherent property of the system, and in geomechanics is typically related to the mean grain size of the material. As we are not aware of any theoretical or numerical demonstrations that such continua fail to regularise the system under the relevant loadings, and in light of the fact that the other regularisation approaches have been demonstrated to fail to do so (at least in certain circumstances), we conclude that the microstructured continuum approach is currently the best choice to produce a model that will regularise the system.

In granular material modelling, microstructured continuum models are most often developed in the Cosserat continuum, as there is a direct physical interpretation of the additional kinematic variable (rigid body micro-rotations) which closely resembles the observed behaviour of grains inside shear bands (Andò et al., 2012; Pinzon et al., 2025). The use of the Cosserat continuum has been further bolstered by micro-mechanical arguments in favour of a non-symmetric stress tensor (Bardet and Vardoulakis, 2001; Papanicolopulos and Veveakis, 2011), a characteristic feature of the continuum. Typically the internal length scale of the continuum is assumed to be a constant and unchanging multiple of the mean grain size d_{50} (Vardoulakis and Papanastasiou, 1988; Papanastasiou and Vardoulakis, 1989, 1992). However, examination of shear bands in crushable granular media, in either field (*e.g.* Rotevatn et al. (2008) and Torabi (2014)) or laboratory (*e.g.* Chambon et al. (2002) and El Bied et al. (2002)) samples demonstrates the presence of a very wide range of grain sizes that evolve under loading, meaning that this assumption is not physically realistic, and a theory describing this grain size evolution is required. This wide range of grain sizes, varying over orders of magnitude, also prevents the usage of discrete element method techniques (Papachristos et al., 2023) to study the problem of particle breakage, as the computational cost of handling the extremely large number of fine particles, the extremely small time step required, and the potential contacts between particles of massively varying size is currently unreasonable. As such, a continuum mechanics theory that is capable of modelling grain breakage would seem to be the best currently available technique to address this problem.

Breakage Mechanics (Einav, 2007a,b) is such a theory, and provides a thermodynamically consistent family of models that describe the evolution of the GSD in terms of an experimentally accessible internal variable B. The theory has been deployed in the development of a wide range of models, from simple models analogous to fracture mechanics theories (Einav, 2007c,d) to more complex models including damage (Das et al., 2014; Tengattini et al., 2014, 2022a,b), porosity (Tengattini et al., 2016) or both (Rossi et al., 2024). The model family has also been extended to the hydrodynamic framework (Alaei et al., 2022), made rate-dependent (Zhang and Buscarnera, 2017; Ray and Buscarnera, 2021, 2025), embedded in a non-local continuum (Nguyen and Einav, 2010), and used to successfully model compaction band formation (Das et al., 2011, 2013).

In a previous work (Collins-Craft et al., 2020), we combined Breakage Mechanics with the Cosserat continuum, to develop a model describing shear bands in crushable granular media. This model features an evolving internal length scale that takes into account the entire GSD, thus rectifying the problem of an unrealistic fixed grain size that was otherwise a feature of Cosserat continuum models in geomechanics. In this paper we further refine this approach by augmenting the capacity to represent volumetric effects that occur due to comminution-driven pore collapse, dilatancy during shearing and density-dependent elasticity. In addition, we add a cohesion to the model that makes it much more suitable to modelling granular rocks by enabling an accurate description of the strength at low confining stresses. The description allows us to capture dilation without particle breakage in the case of low confining

stresses, while also ensuring that under higher confining stresses the model demonstrates pore collapse accompanied by grain breakage. The inclusion of the capacity to dilate also allows us to refine the shear behaviour of the model relative to the previous one, by including a shear strength that varies with the density, as well as the Lode angle. The new model is able to recover the elastic behaviour of the model by Collins-Craft et al. (2020) as a limiting case, as well as one of the end-members of the possible plastic behaviours. Of particular importance in the context of fault mechanics, the internal variable that allows us to capture dilation also gives us sufficient information to calculate the permeability of the system, a quantity that was not accessible in the previous model, which in turn allows us to show the extent of induced permeability changes due to grain crushing, pore collapse and also dilation at the formation of a shear band. While we leave consideration of the thermal, chemical and hydraulic interactions with this mechanical model to future work, we emphasise that the model here presented is capable of predicting fault formation in realistic geological conditions and is suitable for coupling with pore fluid flow, temperature changes and chemical dissolution and precipitation, in order to a develop a comprehensive model of fault behaviour.

2 Cosserat Breakage Mechanics formalism

This section discusses the set of state variables that are needed for characterising the state of a system in the Cosserat Breakage Mechanics framework, suitable for rocks and soils with distinct and crushable grains such as sands and sandstones. The section also introduces the energetic conjugates to the kinematic variables, as well as the equilibrium and boundary conditions that must be respected. All of the state variables and their dependent quantities depend on the spatial position and time, but for the sake of notational simplicity we will not write this dependence explicitly.

2.1 Breakage state variable

In order to express the evolution of the GSD under loading, we make use of the breakage state variable B, which is defined by the ratio of the area between the current GSD, and the initial GSD to the area between the ultimate and initial cumulative GSDs. The concept is illustrated in Figure 1.

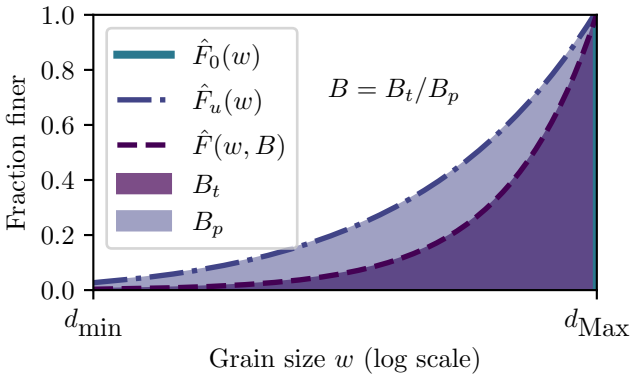

Figure 1: The ratio of two grading areas is used to define the internal breakage variable B, as per Einav (2007b) and Buscarnera and Einav (2012). $\hat{F}_0(w), \hat{F}_u(w)$ and $\hat{F}(w) = (1 - B)\hat{F}_0(w) + B\hat{F}_u$ are the initial, ultimate and current cumulative GSDs respectively for a given grain size w. $d_{\min}$ and d_{Max} are the minimum and maximum grain sizes present in the GSDs.

The maximum grain size d_{Max} remains constant between the initial and ultimate distributions, and $d_{\min}$ is the smallest grain size in the distribution. We take this to be the smallest grain that it is possible to obtain due to comminution, typically understood to be on the order of one micrometre (Kendall, 1978).

We use the universal initial distribution from Buscarnera and Einav (2012), by selecting a Heaviside step function about d_{Max} to express the cumulative initial distribution. The corresponding probability density function of the initial distribution is given by

$$\hat{p}_0(w) = \delta(w - d_{\text{Max}}), \tag{1}$$

where δ represents the Dirac delta function and w a given grain size. We assume that the ultimate GSD follows a power law for its probability density function given by

$$\hat{p}_u(w) = \frac{(3 - \alpha)}{{d_{\text{Max}}}^{3-\alpha} - d_{\min}^{3-\alpha}} w^{2-\alpha}, \tag{2}$$

where α is a dimensionless constant with typical values of $2.5 - 2.7$.

The probability density function for the current GSD is a linear function of B, that expresses the current GSD in relation to the initial and ultimate GSDs:

$$\hat{p}(w,B) = \hat{p}_0(w)(1-B) + \hat{p}_u(w)B. \tag{3}$$

B has a corresponding thermodynamic conjugate, the breakage energy E_B, per Einav (2007b,c).

Within the Cosserat Breakage Mechanics framework, we obtain three non-dimensional grading constants, θ_γ, θ_κ and θ_I, which express "how far apart" the initial and ultimate GSDs are, given by (Collins-Craft et al., 2020)

$$\theta_\gamma = 1 - \frac{3-\alpha}{5-\alpha}\left(\frac{1-(d_{\min}/d_{\mathrm{Max}})^{5-\alpha}}{1-(d_{\min}/d_{\mathrm{Max}})^{3-\alpha}}\right), \tag{4}$$

$$\theta_\kappa = 1 - \frac{3-\alpha}{7-\alpha}\left(\frac{1-(d_{\min}/d_{\mathrm{Max}})^{7-\alpha}}{1-(d_{\min}/d_{\mathrm{Max}})^{3-\alpha}}\right), \tag{5}$$

$$\theta_I = 1 - \frac{3-\alpha}{8-\alpha}\left(\frac{1-(d_{\min}/d_{\mathrm{Max}})^{8-\alpha}}{1-(d_{\min}/d_{\mathrm{Max}})^{3-\alpha}}\right). \tag{6}$$

The θ_γ term controls the energy stored due to elastic straining, the θ_κ term controls the energy stored to elastic curvatures, and the θ_I term controls the angular micro-rotational inertia balance. The details of the derivation of these terms are contained in Collins-Craft et al. (2020). Physically, the higher exponents in the equations of θ_κ and θ_I results in their value being increasingly controlled by the largest grain size present in the GSD. We also note that if the initial GSD is known, it is possible to either calculate a non-zero initial value of B, or to calculate the values of θ_γ, θ_κ and θ_I using the second, fourth and fifth moments of the full distribution.

Finally, it is useful to calculate the harmonic mean grain size of the ultimate GSD (Nguyen and Einav, 2009)

$$d_{Hu} = \left[\frac{3-\alpha}{2-\alpha}\left(\frac{{d_{\mathrm{Max}}}^{2-\alpha} - {d_{\min}}^{2-\alpha}}{{d_{\mathrm{Max}}}^{3-\alpha} - {d_{\min}}^{3-\alpha}}\right)\right]^{-1}, \tag{7}$$

as well as the current harmonic mean grain size as it evolves with B:

$$d_H = \left[(1-B)d_{H0} + Bd_{Hu}\right]^{-1}, \tag{8}$$

where d_{H0} is the harmonic mean of the initial GSD, which is simply given by

$$d_{H0} = d_{\mathrm{Max}}. \tag{9}$$

2.2 Strain and curvature rates

The following derivation adopts the small elastic strain assumption, which is appropriate for the elastic deformation range considered. This does not prevent the total deformation from being arbitrarily large, but assumes that plastic straining constantly relaxes the total straining, keeping the elastic part small (Stathas and Stefanou, 2023). We use index notation and follow the Einstein summation convention. Indices appearing after a comma represent a differentiation with respect to the spatial variable *i.e.* $a_{i,j} = \frac{\partial a_i}{\partial x_j}$. The overdot represents a derivative with respect to time *i.e.* $\dot{a}_i = \frac{\partial a_i}{\partial t}$, with two overdots representing the second derivative.

We define the infinitesimal (nonsymmetric) strain rate tensor by

$$\dot{\gamma}_{ij} = \dot{u}_{i,j} + \epsilon_{ijk}\dot{\omega}^c_k, \tag{10}$$

and the infinitesimal (nonsymmetric) curvature rate tensor by

$$\dot{\kappa}_{ij} = \dot{\omega}^c_{i,j}, \tag{11}$$

where $\dot{u}_i$ and $\dot{\omega}^c_i$ are respectively the rates of translation and rotation along and about the x_i axes and ϵ_{ijk} is the Levi–Civita symbol. These tensors may be decomposed into symmetric and anti-symmetric parts, with the symmetric part of the strain rate tensor being the Cauchy strain rate $\dot{\varepsilon}_{ij}$. We define compression to be positive.

Both strain and curvature rate tensors can be split into trace and deviatoric parts:

$$\dot{\gamma}_{ij} = \frac{1}{3}\dot{\varepsilon}_{kk}\delta_{ij} + \dot{e}_{ij}, \tag{12}$$

$$\dot{\kappa}_{ij} = \frac{1}{3}\dot{\kappa}_{kk}\delta_{ij} + \dot{z}_{ij}, \tag{13}$$

where δ_{ij} is the Kronecker δ, $\dot{\varepsilon}_{kk} = \dot{\varepsilon}_v$ and $\dot{\kappa}_{kk} = \dot{\kappa}_v$.

The strain and curvature rates can be decomposed into elastic (recoverable) and plastic (nonrecoverable) parts within the framework of rate-independent plasticity:

$$\dot{\gamma}_{ij} = \dot{\gamma}^e_{ij} + \dot{\gamma}^p_{ij}, \tag{14}$$

$$\dot{\kappa}_{ij} = \dot{\kappa}^e_{ij} + \dot{\kappa}^p_{ij}. \tag{15}$$

The elastic and plastic parts may also be decomposed into their respective trace and volumetric parts.

2.3 Solid fraction state variable

We adopt the solid fraction ϕ as a state variable, defined by

$$\phi = \frac{\rho}{\rho_s}, \tag{16}$$

where ρ is the bulk density of the material and ρ_s is the solid density. We choose the symbol ϕ for this quantity to align with the usage in the physics community. We also define the relative solid fraction χ (Rubin and Einav, 2011). This variable describes the solid fraction in terms of its position relative to the minimum and maximum values that are possible for a given GSD.

$$\chi = \frac{\phi - \phi_{\min}}{\phi_{\text{Max}} - \phi_{\min}}, \tag{17}$$

where $\phi_{\min}$ and ϕ_{Max} are respectively the minimum and maximum solid fractions for a given value of B. We adopt the expressions of Cil et al. (2020):

$$\phi_{\min} = 1 - \alpha_{\text{lower}}(1-B)^{l_\phi}\exp(-l_\phi B), \tag{18}$$

$$\phi_{\text{Max}} = 1 - \alpha_{\text{upper}}(1-B)^{u_\phi}\exp(-u_\phi B), \tag{19}$$

where α_{lower} and α_{upper} are terms constraining the lower and upper limiting solid densities for unbroken material and l_ϕ and u_ϕ are solid fraction bounds that can be measured experimentally.

2.4 Stresses and couple-stresses

We denote the (nonsymmetric) stress tensor as τ_{ij}, and the couple-stress tensor μ_{ij}, which are conjugate in power with the strain and curvature rates, respectively.

Both of these tensors can also be decomposed into trace and deviatoric parts:

$$\tau_{ij} = \frac{1}{3}\tau_{kk}\delta_{ij} + s_{ij}, \tag{20}$$

$$\mu_{ij} = \frac{1}{3}\mu_{kk}\delta_{ij} + m_{ij}, \tag{21}$$

where $\frac{1}{3}\tau_{kk} = \frac{1}{3}\tau_{ij}\delta_{ij}$ gives the mean stress p. The symmetric part of the stress tensor coincides with the Cauchy stress tensor σ_{ij}.

In addition to the mean stress p we have the deviatoric stress invariant q, and its corresponding deviatoric plastic strain rate invariant $\dot{\gamma}^p$. We use the formulation given in Mühlhaus and Vardoulakis (1987), Vardoulakis and Sulem (1995) and Rattez et al. (2018b) with the appropriate modifications for Breakage mechanics (Collins-Craft et al., 2020):

$$\dot{\gamma}^p = \sqrt{g^\star_1 \dot{e}^p_{ij}\dot{e}^p_{ij} + g^\star_2 \dot{e}^p_{ij}\dot{e}^p_{ji} + {\ell^e}^2(g^\star_3 \dot{z}^p_{ij}\dot{z}^p_{ij} + g^\star_4 \dot{z}^p_{ij}\dot{z}^p_{ji})}, \tag{22}$$

$$q = \sqrt{h^\star_1 s_{ij}s_{ij} + h^\star_2 s_{ij}s_{ji} + \frac{1}{{\ell^e}^2}(h^\star_3 m_{ij}m_{ij} + h^\star_4 m_{ij}m_{ji})}, \tag{23}$$

where g^*_i and h^*_i are weighting factors, the values of which are given in Table 1.

	2D model	3D model
Static model	$g^*_i = \{1/2, 1/6, 1/3, 0\}$	$g^*_i = \{8/15, 2/15, 8/15, 2/15\}$
	$h^*_i = \{9/4, -3/4, 3, 0\}$	$h^*_i = \{2, -1/2, 2, -1/2\}$
Kinematic model	$g^*_i = \{1, -1/3, 4/3, 0\}$	$g^*_i = \{8/9, -2/9, 8/9, -2/9\}$
	$h^*_i = \{9/8, 3/8, 3/4, 0\}$	$h^*_i = \{6/5, 3/10, 6/5, 3/10\}$

Table 1: Values of the coefficients for stress and plastic strain rate invariants in a Cosserat continuum depending on choice of dimension and static or kinematic model.

The expression ℓ^e is the energetic length scale defined in Collins-Craft et al. (2020) and given by

$$\ell^e = d_{\text{Max}}\sqrt{1-\theta_\kappa B}. \tag{24}$$

The Cosserat material length is no longer a constant as in Mühlhaus and Vardoulakis (1987), but depends on the entire GSD through the grading constant θ_κ and evolves as the distribution evolves with B.

2.5 Equilibrium and boundary conditions

We consider a three-dimensional body $\mathcal{V}$, with a boundary $\partial\mathcal{V}$ and a moment of micro-rotational inertia I_{ij}. We denote the part of the boundary with Dirichlet boundary conditions as $\partial\mathcal{V}_D$, with prescribed velocities $\bar{\dot{u}}_i$ and rotation rates $\bar{\dot{\omega}}_i^c$, while the part of the boundary with Neumann boundary conditions is denoted as $\partial\mathcal{V}_N$, with prescribed surface tractions $\bar{\tau}_i$ and surface couples $\bar{\mu}_i$. Body forces f_i and body couples b_i apply everywhere in $\mathcal{V}$. The equations of motion and equilibrium equations on $\mathcal{V}$ are then (Germain, 1973):

$$\begin{cases} \tau_{ij,j} - f_i = \rho\ddot{u}_i, \\ \mu_{ij,j} - \epsilon_{ijk}\tau_{jk} - b_i = I_{ij}\ddot{\omega}_j^c, \\ \partial\mathcal{V}_D \cup \partial\mathcal{V}_N = \partial\mathcal{V}, \\ \partial\mathcal{V}_D \cap \partial\mathcal{V}_N = \varnothing, \\ \bar{\tau}_i = \tau_{ij}\bar{n}_j \text{ and } \bar{\mu}_i = \mu_{ij}\bar{n}_j \text{ on } \partial\mathcal{V}_N, \\ \dot{u}_i = \bar{\dot{u}}_i \text{ and } \dot{\omega}_i^c = \bar{\dot{\omega}}_i^c \text{ on } \partial\mathcal{V}_D, \end{cases} \tag{25}$$

where $\bar{n}_j$ are the components of the normal unit vectors on $\partial\mathcal{V}$ and $\varnothing$ is the empty set.

3 Constitutive model

Having detailed the state variables that will be used in this work, we can now move to the specification of a particular model in the Cosserat Breakage Mechanics family. We specify only the essential elements of the new model, while leaving the detailed derivation of the model quantities to Appendix A, and the details of its numerical implementation to the supporting information §4.

We start by proposing an internal energy (per unit volume) following a limit case of the internal energy presented in Riley et al. (2025). Unlike those authors, we ignore any consideration of pressure-dependent stiffness for the sake of simplicity, as this effect is mainly important at much lower values of confining stress than what we consider in this work. The energy potential with a suitable modification for the Cosserat continuum is:

$$\hat{\mathcal{U}}(\gamma_{ij}^e, \kappa_{ij}^e, \rho, B) = \left(\frac{\rho}{\rho_s^\star}\right)^n \left(\frac{1}{2}(1-\theta_\gamma B)C_{ijkl}^e\gamma_{ij}^e\gamma_{kl}^e + \frac{1}{2}(1-\theta_\kappa B){d_{\text{Max}}}^2 D_{ijkl}^e\kappa_{ij}^e\kappa_{kl}^e\right), \tag{26}$$

where $\rho_s^\star$ is the unstressed solid density that is a fixed material constant, n is the degree of nonlinearity in the density, and

$$C_{ijkl}^e = \left(\bar{K} - \frac{2\bar{G}}{3}\right)\delta_{ij}\delta_{kl} + (\bar{G}+\bar{G}_c)\delta_{ik}\delta_{jl} + (\bar{G}-\bar{G}_c)\delta_{il}\delta_{jk}, \tag{27}$$

$$D_{ijkl}^e = \left(\bar{L} - \frac{2\bar{H}}{3}\right)\delta_{ij}\delta_{kl} + (\bar{H}+\bar{H}_c)\delta_{ik}\delta_{jl} + (\bar{H}-\bar{H}_c)\delta_{il}\delta_{jk}. \tag{28}$$

$\bar{K}$, $\bar{G}$, $\bar{G}_c$, $\bar{L}$, $\bar{H}$ and $\bar{H}_c$ are the nonlinear analogues of the corresponding terms in linear Cosserat elasticity. If we set $n = 0$, we recover classical linear Cosserat elasticity without any consideration of density dependence. We can use the same calibration relationships developed in Collins-Craft et al. (2020) to obtain the values of $\bar{G}_c$, $\bar{H}$ and $\bar{H}_c$, under the same assumption of $\bar{L} = 0$. Non-zero values of n allow us to recover the observed dependence of stiffness on the density of the material (Hardin and Drnevich, 1972). From this potential we are able to derive the elastic stress and couple stress, the chemical potential and thermodynamic pressure, as well as the breakage energy by following the standard procedures detailed in Appendix A.

We suppose that the yield surface of the material is given by

$$y = \left(\sqrt{\frac{E_B}{E_c}}(1-B) - \zeta\chi\right)^2 + \left(\frac{q}{Mp^e + \phi(1-B)c}\right)^2 - 1 \leq 0, \tag{29}$$

where M is the stress ratio in the $p-q$ plane given by a function specified below, E_c is the critical breakage energy, c is the cohesion of the material, and ζ is a material parameter that controls the potential to dilate, and ranges from 0

(no dilation) to 1 (maximally dilating). We note that in the case where we set $c = 0$ and $\zeta = 0$, we recover the yield surface given in Collins-Craft et al. (2020).

We postulate that the plastic evolution rules of the system are given by (Tengattini et al., 2016)

$$\dot{B} = \lambda \langle F \rangle \frac{2(1-B)}{\sqrt{E_B E_c}} \cos^2(\omega), \tag{30}$$

$$\dot{\phi}^p = \lambda F \frac{2\phi(1-B)}{p^e} \sqrt{\frac{E_B}{E_c}} \sin^2(\omega), \tag{31}$$

$$\dot{\gamma}^p_s = \lambda \frac{2q}{(Mp^e + \phi(1-B)c)^2}, \tag{32}$$

where $\langle \cdot \rangle = (\cdot + |\cdot|)/2$ are Macaulay brackets, and F is a function given by

$$F = \sqrt{\frac{E_B}{E_c}}(1-B) - \zeta\chi, \tag{33}$$

and ω is a coupling angle that allocates dissipation between plastic volumetric straining and grain breakage given by

$$\omega = \frac{\pi}{2}(1 - \chi \mathcal{H}(F)), \tag{34}$$

where $\mathcal{H}(\cdot)$ is the Heaviside step function, defined such that

$$\mathcal{H}(x) = \begin{cases} 0 & \text{if } x < 0, \\ 1 & \text{if } x \geq 0. \end{cases} \tag{35}$$

Tengattini et al. (2016) demonstrated the model's ability to represent crushable granular soils that can experience dilation. We generalise their rules slightly to include cohesion in the expression for the shear strain rate invariant, allowing us to model granular rocks in addition to granular soils. We can use (63) of Appendix A.1 to transform (31) into an expression for $\dot{\varepsilon}^p_v$, as well as the derivative of (32) with respect to the plastic deviatoric strain and curvature rates to deduce the flow rule for the complete set of plastic strain and curvature rates:

$$\dot{\gamma}^p_{ij} = \lambda \left[F \frac{2(1-B)}{3p^e} \sqrt{\frac{E_B}{E_c}} \sin^2(\omega)\delta_{ij} + \frac{2}{(Mp^e + \phi(1-B)c)^2} \left(h^\star_1 s^e_{ij} + h^\star_2 s^e_{ji} \right) \right], \tag{36}$$

$$\dot{\kappa}^p_{ij} = \lambda \frac{2}{[\ell(Mp^e + \phi(1-B)c)]^2} \left(h^\star_3 m_{ij} + h^\star_4 m_{ji} \right). \tag{37}$$

As is well-known, densely-packed sands dilate under shear, and the function F allows the model to express how the behaviour changes as the density and GSD evolves. When $F < 0$ the system dilates due to grain rearrangement without grain breakage *i.e.* the rate of breakage $\dot{B} = 0$ and the plastic rate of the solid fraction $\dot{\phi}^p < 0$. We refer to this as the dilative side of the critical state line. When $F > 0$ grains break and the solid fraction increases *i.e.* $\dot{B} > 0$ and $\dot{\phi} > 0$. We will refer to this as the compactive side of the critical state line. When $F = 0$ we are in a state of zero breakage growth and isochoric plastic straining, *i.e.* the critical state. In this model, the critical state appears at a lower confining stress than the peak deviatoric stress. The mathematical form of (34) allows us to guarantee all the volumetric straining goes to solid fraction changes when $F < 0$, while smoothly varying the allocation between grain breakage and pore collapse when $F > 0$. This is a point of contrast with the model specified in Collins-Craft et al. (2020), where ω is a fixed material constant that does not evolve in time, and dilation cannot occur.

We take M to be dependent on the position of the state relative to the critical state by:

$$M = M_0[1 + \zeta \mathcal{H}(-F)F]. \tag{38}$$

Thus, where our system is dense M is larger, while looser systems have a correspondingly lower value of M, matching experimental observations (Bolton, 1986; Wichtmann, 2016). M_0 is given by another function

$$M_0 = \frac{3\sin(\varphi)}{\sqrt{3}\cos(\beta) - \sin(\beta)\sin(\varphi)}, \tag{39}$$

where φ is the internal friction angle (a material parameter with $\varphi \geq 0$) and β is the Lode angle. Experimental and theoretical results have shown that the Lode angle plays a role in the localisation behaviour of rocks such as sandstones (Couture and Bésuelle, 2022, 2023). In the Cosserat continuum, this angle may be defined as:

$$\beta = \frac{1}{3} \arcsin \left(\frac{27}{2} \frac{\det(s_{ij})}{q^3} \right), \tag{40}$$

and classically lies between $-\pi/6$ and $\pi/6$ (Papamichos, 2010). We use the definition such that in triaxial compression the Lode angle is equal to $\pi/6$.

Finally, we must make a constitutive assumption about the evolution of the solid density. Most commonly, solids are assumed to have a fixed density, but here we consider its inevitable change driven by elastic volumetric straining. We follow Alaei et al. (2021) in specifying

$$\dot{\rho}_s = \rho_s \chi \dot{\varepsilon}_v^e. \tag{41}$$

The model is now fully specified, with the detailed derivations and the proof of the non-negativity of the rate of dissipation (as required by the second law of thermodynamics) presented in Appendix A. We note here in passing that by setting $n = 0$, $c = 0$, $\zeta = 0$ and $\chi = 1$ we can recover the model specified in Collins-Craft et al. (2020) for $\bar{\omega} = 0°$ and loading at constant volume. For any other system values or different load conditions, we will recover different behaviour due to the changes that we have made to the volumetric parts of the model.

4 Parametric study

4.1 Calibration

We calibrate the proposed model against Bentheim sandstone, which has been the subject of extensive experimental studies, and has a large-grained composition of approximately 95% quartz (Klein et al., 2001), which is ideal for demonstrating the capabilities of the model. We assume samples to start in an unbroken state ($B = 0$) and choose an initial relative solid fraction of $\chi_0 = 0.5$, so that in combination with the upper and lower bound given below in Table 2, the initial solid fraction $\phi_0 = 0.775$. We select the potential to dilate $\zeta = 0.5$ as the middle value of its possible range. We then obtain the other parameter values from the literature, either directly or via back-calibration using our chosen initial values for the state variables and the parameter ζ.

The minimum grain $d_{\min} = 1$ μm size is chosen following arguments in Kendall (1978) and Buscarnera and Einav (2012). The maximum grain size d_{Max} is as reported for Bentheim sandstone in Klein et al. (2001). α is chosen in line with studies of the GSDs of mature faults (Sammis et al., 1986, 1987; Sammis and Biegel, 1989; An and Sammis, 1994). The derived granulometric parameters are then calculated via (4), (5) and (6). The lower and upper limit leading terms are estimates of the plausible range based on the reported porosities in Klein et al. (2001) (22.8%) and Noël et al. (2021) (24.0%). The upper and lower solid fraction bounds are taken directly from Cil et al. (2020), in the absence of any experimental evidence on what the appropriate values would be for this sandstone. The density nonlinearity index is chosen to be 3, in line with Alaei et al. (2022). In general this index can be calibrated against standard triaxial compression tests. The nonlinear bulk and shear moduli are taken from the values reported in Noël et al. (2021), divided by their reported solid fraction raised to the density nonlinearity index. These can be obtained either by fitting to the load-displacement curve of standard triaxial compression tests, or using p- and s-wave velocities. We use the three-dimensional kinematic Cosserat model, which determines the values of $g_i^\star$ and $h_i^\star$. $\bar{L}$ is set to zero as we do not expect the torsional effects to play any role in our intended application. We then use the calibration relationships derived in Collins-Craft et al. (2020), which give the values of $\bar{G}_c$, $\bar{H}$ and $\bar{H}_c$ by

$$\bar{G}_c = \frac{3\bar{G}}{2(h_1^\star - h_2^\star)}, \tag{42}$$

$$\bar{H} = \frac{3\bar{G}}{2(h_3^\star + h_4^\star)}, \tag{43}$$

$$\bar{H}_c = \frac{3\bar{G}}{2(h_3^\star - h_4^\star)}, \tag{44}$$

The density of the solid material is taken by dividing the reported bulk density in Noël et al. (2021) by their reported solid fraction, two quantities that can be measured by weighing samples when both dry and wet. The solid fraction can also be obtained by x-ray micro-computed tomography (μ-CT) scans where available.

This leaves us three remaining constants to calibrate using experiments. E_c is typically obtained from an isotropic volumetric compaction test and finding the point at which the grains start to break, a quantity often denoted $P^\star$ in the literature. Using the initialisation method given in supporting information §3, the set of state variables corresponding to this stress state can be obtained, and the value of E_B can thus be calculated. As $q = 0$ at this point, (29) can be rearranged in terms of E_c to give

$$E_c = \frac{E_B(1-B)^2}{(1+\zeta\chi)^2}. \tag{45}$$

In our case we take the value of the crushing pressure given in Klein et al. (2001) (390 MPa) as $P^\star$, noting that for their samples of Bentheim sandstone they report an initial solid fraction of 0.772 (corresponding to $\chi_0 = 0.44$). We

thus use this value as the solid fraction in the stress-free state for the calibration, rather than our assumed initial value of 0.775 (corresponding to $\chi_0 = 0.5$). Calculating the corresponding set of state variables for $P^\star$, we calculate E_B and χ at this state and obtain our value of E_c by substituting them in to (45).

φ can be obtained by observing the ratio between p and q in a triaxial test when the system enters the critical state, while c can be determined by using lines-of-best fit from triaxial compression tests done at very low confining stresses. Here, we obtain φ and c by a standard least squares fitting procedure that minimises the norm of y evaluated at each experimental data point. We use the results of the triaxial compression tests reported for Bentheim sandstone in Klein et al. (2001), Klein and Reuschlé (2003) and Baud et al. (2006) as the source of the calibration data, taking the values reported at "the onset of dilatancy" (and using *PlotDigitizer* (2025) to extract the relevant data from Figure 5 of Klein et al. (2001)), and excluding the isotropic compaction tests. The final set of obtained calibrated values is contained in Table 2.

Basic granulometric parameters			
Minimum grain size	$d_{\min}$	0.001	mm
Maximum grain size	d_{Max}	0.5	mm
Ultimate GSD exponent	α	2.6	
Derived granulometric parameters			
First grading index	θ_γ	0.818	
Second grading index	θ_κ	0.901	
Third grading index	θ_I	0.919	
Porosimetric parameters			
Upper limit leading term	α_{upper}	0.2	
Lower limit leading term	α_{lower}	0.25	
Upper solid fraction bound	u_ϕ	0.12	
Lower solid fraction bound	l_ϕ	0.16	
Mechanical parameters			
Density nonlinearity index	n	3	
Nonlinear bulk stiffness	$\bar{K}$	19363	MPa
Nonlinear shear stiffness	$\bar{G}$	15718	MPa
Cosserat kinematic model h_i parameters	$\{h_1^\star, h_2^\star, h_3^\star, h_4^\star\}$	$\{6/5, 3/10, 6/5, 3/10\}$	
Cosserat kinematic model g_i parameters	$\{g_1^\star, g_2^\star, g_3^\star, g_4^\star\}$	$\{8/9, -2/9, 8/9, -2/9\}$	
First nonlinear Cosserat shear stiffness	$\bar{G}_c$	26197	MPa
Nonlinear Cosserat torsion stiffness	$\bar{L}$	0	MPa
Second nonlinear Cosserat shear stiffness	$\bar{H}$	15718	MPa
Third nonlinear Cosserat shear stiffness	$\bar{H}_c$	26197	MPa
Unstressed solid mass density	$\rho_s^\star$	2.645×10^{-3}	g/mm^3
Critical breakage energy	E_c	3.21	MPa
Internal friction angle	φ	0.612	
Cohesion	c	21.5	MPa
Potential to dilate	ζ	0.5	

Table 2: Calibrated parameter values for the model developed in this paper.

To demonstrate the capabilities offered by the proposed model, we compare it with the model detailed in Collins-Craft et al. (2020), which entails calibrating that model against the same data. We note that the model in Collins-Craft et al. (2020) does not possess certain parameters or their equivalents (namely, the porosimetric terms, the density nonlinearity index, the unstressed solid mass density and the cohesion). In the newly proposed model, M and ω are functions of the state, the parameter φ is calibrated against data and the parameter ζ is chosen to be in the middle of its possible range. In the previous model from Collins-Craft et al. (2020), $\bar{M}$ is a parameter that we calibrate against data and $\bar{\omega}$ is a parameter chosen to be in the middle of its possible range. We add a bar to distinguish between the usages of these quantities as variables and parameters, and further distinguish $\bar{\omega}$ by reporting its value in degrees, while the variable ω is in radians.

We set the bulk stiffness K and shear stiffness G to have the same values in the original model as the effective nonlinear stiffness of the new model at 200 MPa. We obtain E_c in a conceptually similar fashion to the new model (by calculating the state variables at the crushing pressure, calculating the value of E_B corresponding to these variables, rearranging the yield function to make E_c the subject and substituting in the appropriate values). We obtain $\bar{M}$ by varying its value and minimising the norm of y against the experimental data, in the same fashion as φ and c were obtained for the new model. The full set of calibrated values for the model presented in Collins-Craft et al. (2020) are given in Table 3.

Basic granulometric parameters			
Minimum grain size	$d_{\min}$	0.001	mm
Maximum grain size	d_{Max}	0.5	mm
Ultimate GSD exponent	α	2.6	
Derived granulometric parameters			
First grading index	θ_γ	0.818	
Second grading index	θ_κ	0.901	
Third grading index	θ_I	0.919	
Mechanical parameters			
Bulk stiffness	K	9.58×10^3	MPa
Shear stiffness	G	7.78×10^3	MPa
Cosserat kinematic model h_i parameters	$\{h_1^\star, h_2^\star, h_3^\star, h_4^\star\}$	$\{6/5, 3/10, 6/5, 3/10\}$	
Cosserat kinematic model g_i parameters	$\{g_1^\star, g_2^\star, g_3^\star, g_4^\star\}$	$\{8/9, -2/9, 8/9, -2/9\}$	
First Cosserat shear stiffness	G_c	13.0×10^3	MPa
Cosserat torsion stiffness	L	0	MPa
Second Cosserat shear stiffness	H	7.78×10^3	MPa
Third Cosserat shear stiffness	H_c	13.0×10^3	MPa
Critical breakage energy	E_c	6.50	MPa
Slope of the critical state line in the $p-q$ plane	$\bar{M}$	2.04	
Coupling angle	$\bar{\omega}$	45	$^\circ$

Table 3: Calibrated parameter values for the model presented in Collins-Craft et al. (2020).

The yield surfaces obtained using the calibrated values (with $\phi = 0.772$ for the model presented in this paper) against the experimentally obtained values are shown in Figure 2.

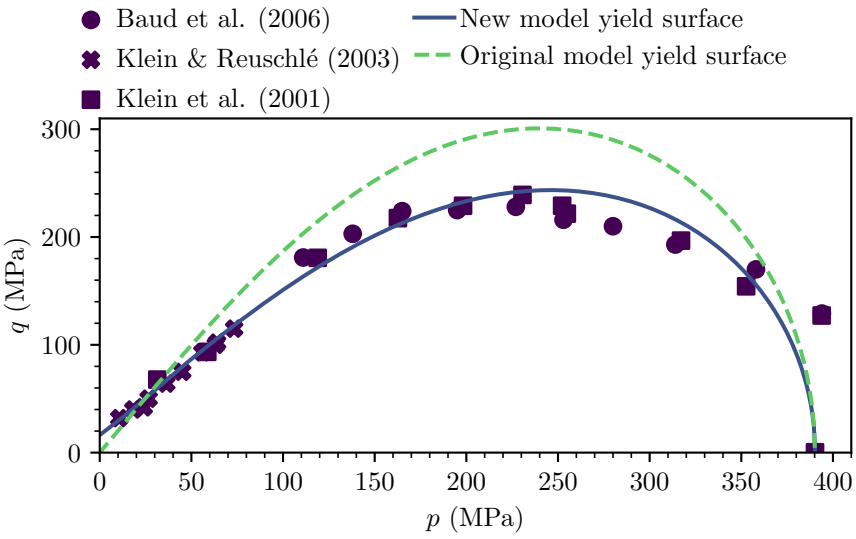

Figure 2: Yield surfaces of the model presented in this paper and the model presented in Collins-Craft et al. (2020), and the experimental values from Klein et al. (2001), Klein and Reuschlé (2003) and Baud et al. (2006) used to calibrate the relevant parameters.

Figure 2 shows that the new model is able to fit the experimental data substantially better than the original model. The tests done at low confinement stresses clearly point towards Bentheim sandstone having cohesion, which the new model accommodates, while the original model cannot. Also visible in the experimental data is a slight non-convexity of the yield surface at low confining stresses, which only the new model can match. In general, we are not aware of any previously developed model that has been fitted to these data points that could recover this observation, and very often classical plasticity models insist on the convexity of the yield surface. This restriction can be lifted without affecting the non-negativeness of the rate of dissipation, as demonstrated in Appendix A.1. As such, we conclude that the new model more accurately describes the initiation of plasticity than the original model, at low, intermediate and high ranges of confining stress.

We observe how the yield surface of the new model changes as we vary the breakage index and the relative solid fraction, in Figure 3.

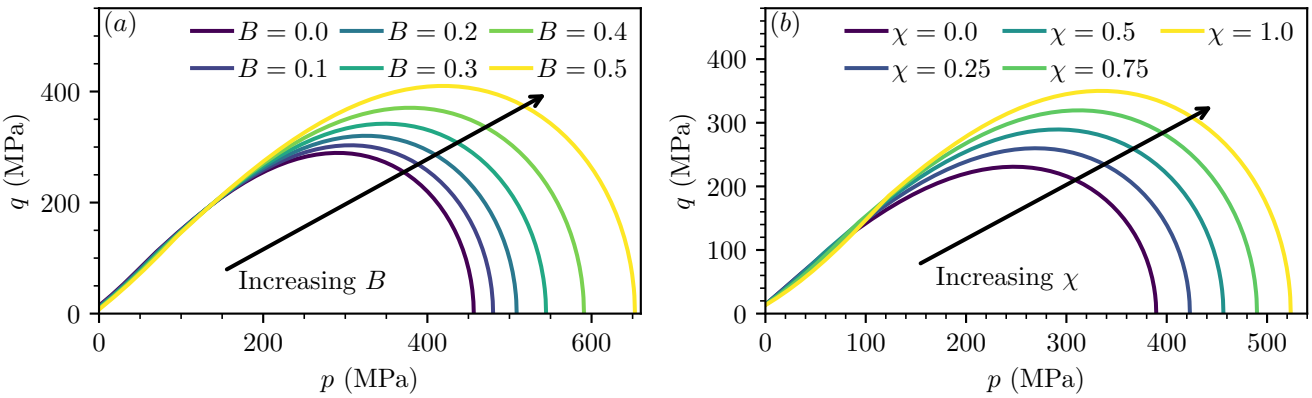

Figure 3: The changes in the yield surface in $p - q$ space as (a) the breakage is varied from 0 to 0.5 in increments of 0.1 and as (b) the relative solid fraction is varied from 0 to 1 in increments of 0.25.

As the breakage value increases, the yield surface grows steadily larger and moves rightward, with decreasing shear strength before yield at lower confining stresses and increasing shear capacity at higher confining stresses. This is the same pattern as for the model in Collins-Craft et al. (2020), other than an absence of decrease of shear strength at low confining stresses. Similarly, as the solid fraction is increased the yield surface also enlarges, although the effect on the shear behaviour is much smaller than that of the breakage index.

We can also examine the effect of changing the parameter ζ, the tendency to dilate, on the system, varying from $\zeta = 0$ (minimal dilation) to $\zeta = 1$ (maximal dilation), and shown in Figure 4.

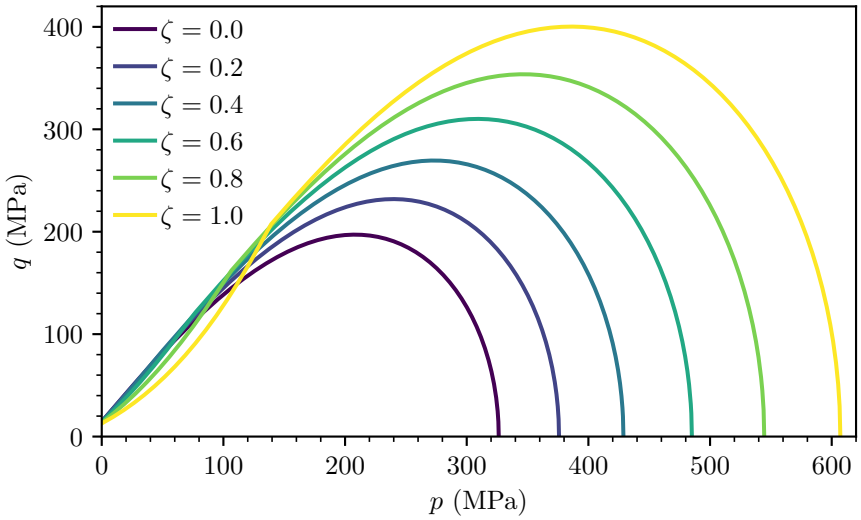

Figure 4: The changes in the yield surface in $p - q$ space as ζ is varied from 0 to 1 in increments of 0.2.

The degree of non-convexity in Figure 4 changes with ζ. This is a necessary consequence of the system softening with dilation, in a manner analogous to the softening with increasing wetting in unsaturated soil mechanics, where non-convex yield surfaces are common (Sheng et al., 2008). The point at which the convexity of the yield surface changes does not require any special numerical treatment to deal with the nonsmooth behaviour, as both $\dot{B}$ and $\dot{\phi}^p$ will be zero at this point and so only the shear plastic flow component will be non-zero.

4.2 Comparison with the drained triaxial tests of Klein et al. (2001)

In order to validate the performance of our model and demonstrate its advantages as compared to the model developed in Collins-Craft et al. (2020), we conduct a comparison with the drained triaxial compression tests on Bentheim sandstone performed by Klein et al. (2001). The relevant loading conditions are shown in Figure 5.

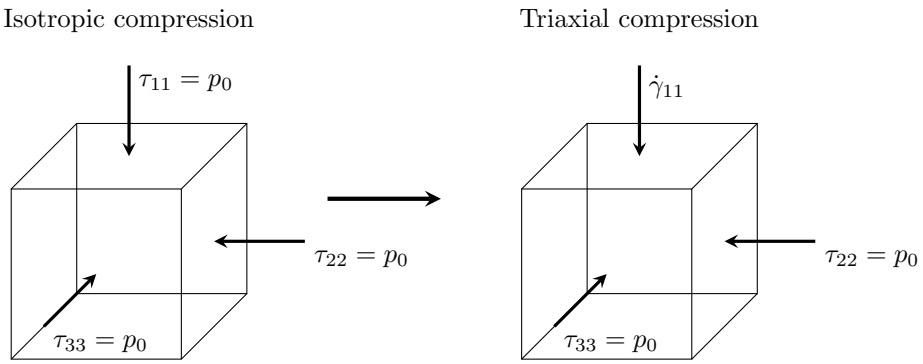

Figure 5: The two stages of the drained triaxial compression test: isotropic compression with $\tau_{11} = \tau_{22} = \tau_{33}$ until the target confining stress is reached followed by triaxial compression with $\tau_{22} = \tau_{33}$ at the target confining stress and axial loading provided at a fixed strain rate. All curvatures and couple-stresses are fixed to zero during both deformation phases.

We set the parameters of our new model to those described in Table 2, with the initial solid fraction in the stress-free configuration set to $\phi = 0.772$. We similarly set the parameters of the original model to those reported in Table 3. The data sets for comparison are taken from Figure 3(a) of Klein et al. (2001), digitised with *PlotDigitizer* (2025) by selecting the points at which markers are plotted. For each confining stress, we perform the isotropic compression to the target confining stress p_0 in one step, obtaining the corresponding elastic strains analytically for the original model ($\gamma_{11/22/33} = p_0/3K$), and numerically obtaining the elastic strains, density and solid fraction for the new model following the method described in supporting information §3, and choosing to update ϕ_0. For each test, we start the simulation after the initial state has been obtained, and we load the sample under controlled axial strain γ_{11} up to 0.12 using the numerical methods detailed in supporting information §4.

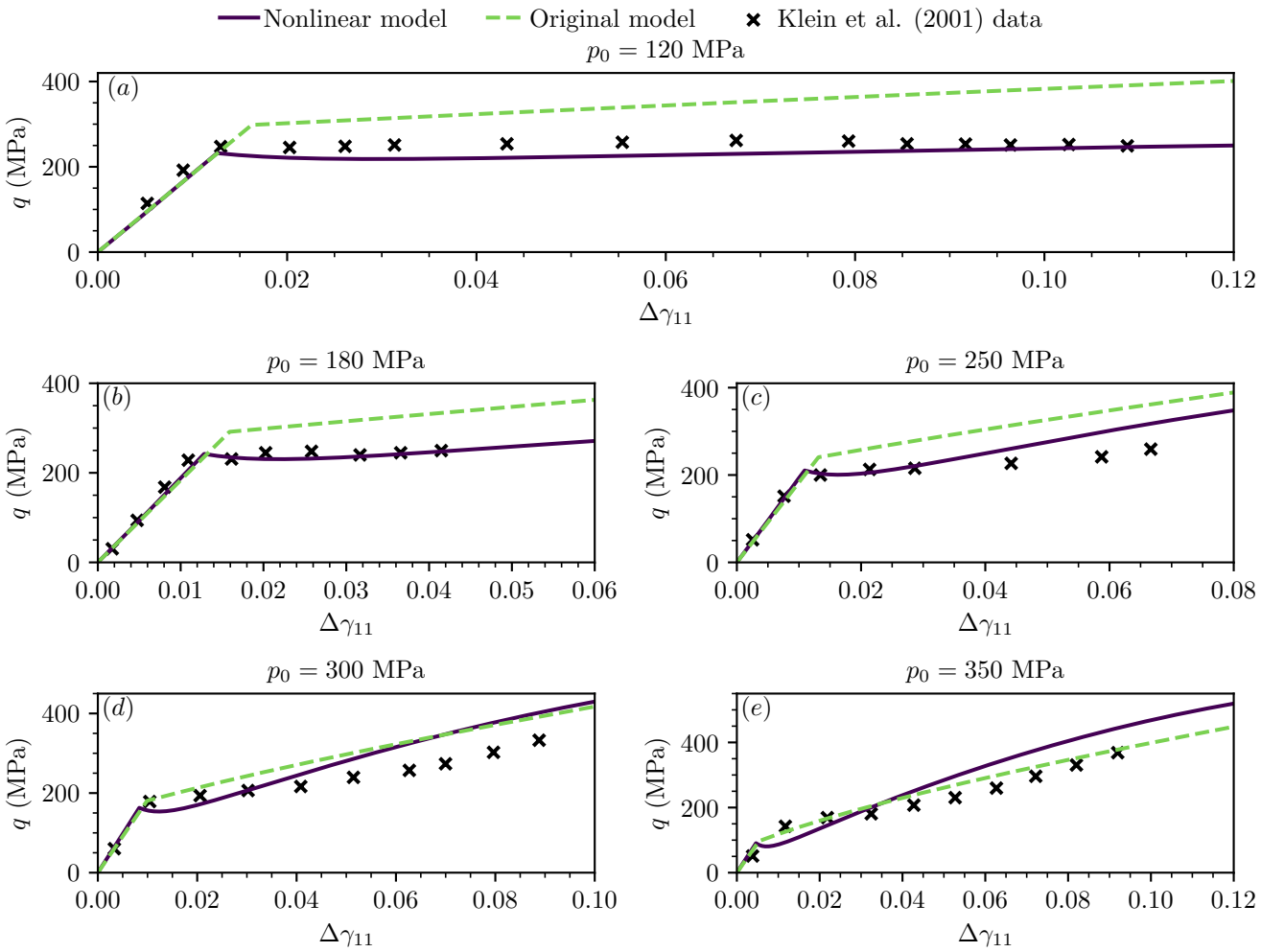

Figure 6: Comparison of the predictions of the new and original model during drained triaxial compression with experimental data from Klein et al. (2001), for (a) 120 MPa confining pressure, (b) 180 MPa confining pressure, (c) 250 MPa confining pressure, (d) 300 MPa confining pressure, and (e) 350 MPa confining pressure.

In Figure 6, we truncate the simulation results to extend slightly further than the experimental data points for each simulation. We observe that the performance of the new model is able to capture the transition between the relatively flat stress-strain curves observed at lower confining pressures to those that feature apparent hardening at higher confining pressures. Visible in the new model are small instances of apparent softening (or "brittleness") that the original model (which is always hardening) is unable to reproduce. Small drops in the stress-strain curve are observed experimentally in what is often referred to as the "shear-enhanced compaction" regime, are associated with the formation of compaction bands, and have been observed in Bentheim sandstone (*e.g.* in Klein et al. (2001) and Baud et al. (2006)), Bleurswiller sandstone (Heap et al., 2015), Tuffeau de Maastricht (Wu et al., 2019) and artificial rocks formed from glass beads (Carbillet et al., 2022), among others. The ability to predict the experimental stress-strain curve of real rocks when the original model could not, demonstrates the importance of the more sophisticated volumetric behaviour in the model developed in this paper.

4.3 Simulations and stability analysis of shear tests

In order to understand the mechanical behaviour as well as the localisation tendency of the system we consider two loading cases, shearing at constant volume, which approximates the fast undrained shear that faults typically experience, and shearing at constant confining stress, which approximates the behaviour of the system under slow drained loading. Per Sulem et al. (2011) 200 MPa is a representative pressure for the depth at which seismic faulting typically occurs, so we choose this as our central value for the initial confining pressure in both load cases. We confine the system uniformly (that is $\gamma^e_{11} = \gamma^e_{22} = \gamma^e_{33}$ at the start of the simulation, using the initialisation method described in supporting information §3, without adjusting the imposed solid fraction value) and simulate from this point while maintaining the appropriate boundary condition while applying 0.2 strain in the γ_{12} and γ_{21} entries, using the numerical methods detailed in supporting information §4. We show the relevant loading conditions in Figure 7.

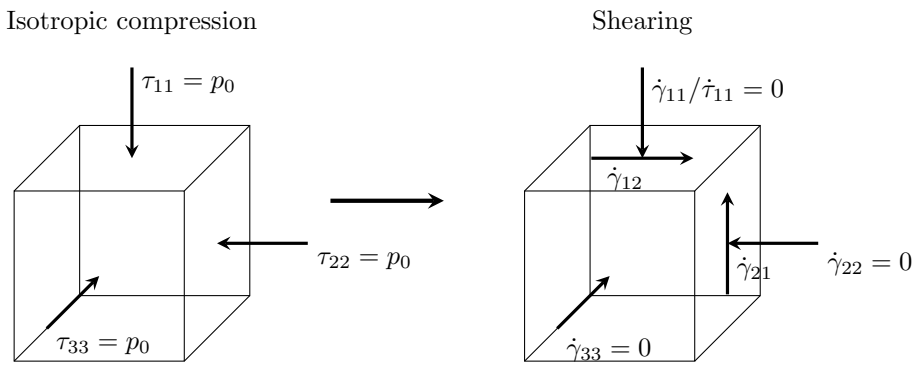

Figure 7: The two stages of the confined shearing test: isotropic compression with $\tau_{11} = \tau_{22} = \tau_{33}$ until the target confining stress is reached followed by shearing applied to $\dot{\gamma}_{12/21}$ with $\dot{\gamma}_{22} = \dot{\gamma}_{33} = 0$, starting at the strains associated with the target confining stress. When shearing under constant volume $\dot{\gamma}_{11} = 0$, when shearing under constant confining stresses $\dot{\tau}_{11} = 0$. All curvatures and couple-stresses are fixed to zero during both deformation phases.

Once the results of each simulation have been obtained, a linear stability analysis is conducted where the system is perturbed and we study whether the perturbations grow or decay in time. We fix the perturbation to be horizontal *i.e.* $\tilde{n}_i = \{1, 0, 0\}$, as analyses allowing the band orientation to vary have shown this to be the orientation with the fastest growth rate. An eigenvector analysis is also undertaken to qualitatively characterise the nature of the shear band. These procedures are detailed in supporting information §2.

4.3.1 Sensitivity to χ

Changing the initial value of the relative solid fraction χ_0 allows us to study the effect of changing the initial volumetric behaviour of the new model. In the original model, we can change the values of $\bar{\omega}$ to similarly vary the volumetric behaviour. The results of these simulations are shown in Figure 8 for constant volume shearing.

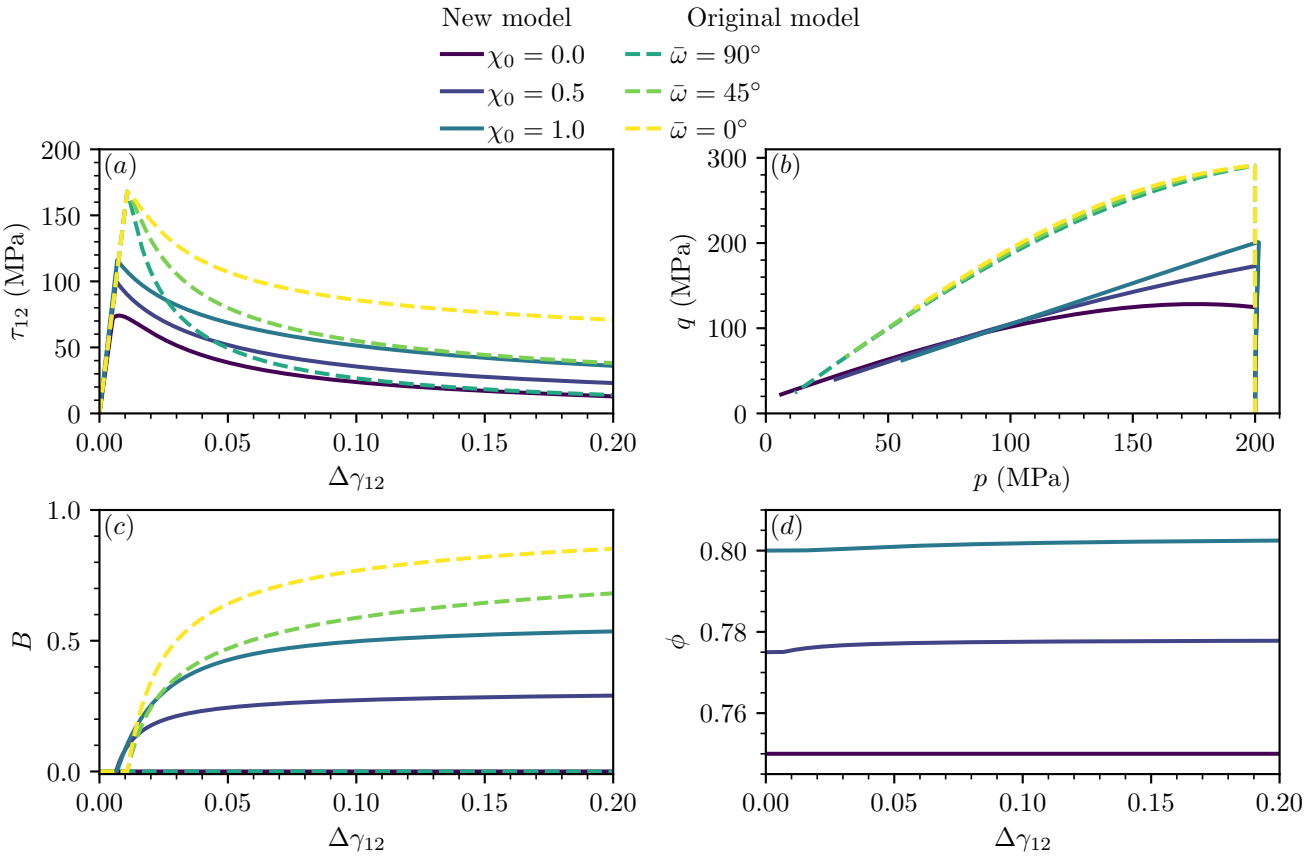

Figure 8: The results of simulations of shearing at constant volume with an initial confining stress of 200 MPa, using the model presented in this paper ($\chi \in \{0.0, 0.5, 1.0\}$) and the model presented in Collins-Craft et al. (2020) ($\bar{\omega} \in \{0°, 45°, 90°\}$). (a) The shear stress τ_{12} against the increment of shear strain $\Delta\gamma_{12}$, (b) the deviatoric stress invariant q against the mean stress p, (c) the breakage index B against the increment of shear strain $\Delta\gamma_{12}$, and (d) the solid fraction ϕ against the increment of shear strain $\Delta\gamma_{12}$. The quantity ϕ does not exist in the original model, and hence only the new model is shown in subfigure (d).

Figure 8 demonstrates that under varying χ_0 or $\bar{\omega}$, the trends remain broadly similar. As χ_0 increases, the stress that can be sustained prior to yielding also increases slightly. By contrast, variations in $\bar{\omega}$ have no impact on the point at which yielding first occurs. For all values of χ_0, the apparent softening experienced by the system is substantially less than for the corresponding system in the original model, although the general trends are similar (a coupling angle $\bar{\omega}$ favouring dissipation by plastic volumetric straining ($\bar{\omega} = 90°$) shows more apparent softening than $\bar{\omega}$ favouring dissipation by grain breakage ($\bar{\omega} = 0°$), likewise a relative solid fraction χ_0 that favours volumetric compaction shows more apparent softening than χ_0 favouring grain breakage). The original model displays substantially more grain breakage after a modest amount of shearing than the new model. The interaction between grain breakage and solid fraction in the new model allows the system to approach the critical state where the breakage state variable will stop evolving. The original model has a critical state at $B = 1$, while in the new model the F function allows the critical state to be approached at any value of B. Hence, the new model is able to much more accurately model the real physical behaviour of granular media, which can enter the critical state without requiring that the GSD has reached its ultimate state. This has been demonstrated in Tengattini et al. (2016), where an extensive comparison with experimental results was undertaken. For the solid fraction variable that is only available within the new model, we see very little change in the value of the solid fraction, as is expected for constant volume loading conditions. We conclude that while both models demonstrate variable volumetric behaviour, the new model changes in a comparatively more stable way without extremely rapid increases in the value of the breakage index. Finally, the new model arrives at the yield surface at smaller values of stress and strain, due to the better fitting of the yield surface to the experimental results. Further variables of interest from these simulations are shown in supporting information Figure S.1.

The sensitivity to changes in the relative solid fraction χ_0 and the coupling angle $\bar{\omega}$ can likewise be studied for constant confining stress, shown in Figure 9.

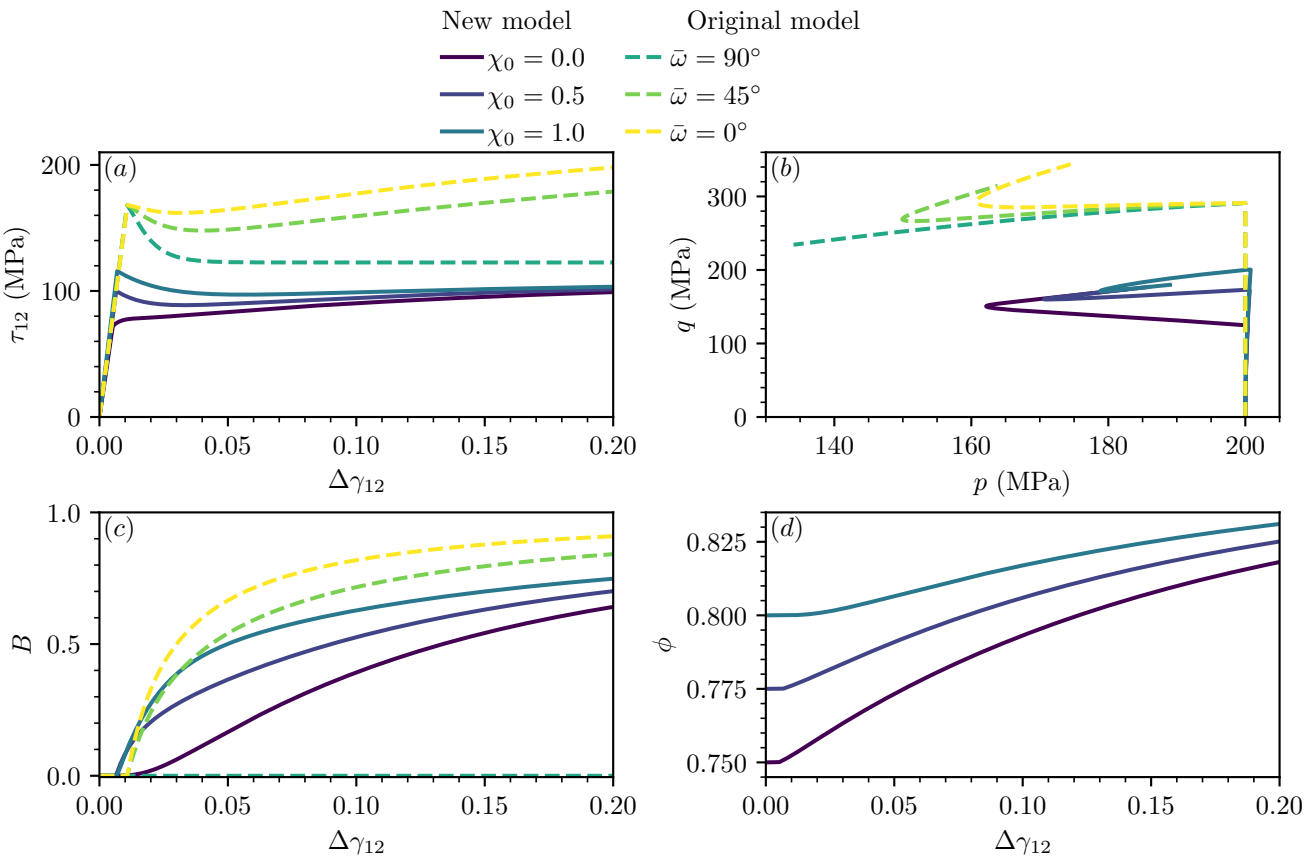

Figure 9: The results of simulations of shearing at constant confining stress of 200 MPa, using the model presented in this paper ($\chi \in \{0.0, 0.5, 1.0\}$) and the model presented in Collins-Craft et al. (2020) ($\bar{\omega} \in \{0°, 45°, 90°\}$). (a) The shear stress τ_{12} against the increment of shear strain $\Delta\gamma_{12}$, (b) the deviatoric stress invariant q against the mean stress p, (c) the breakage index B against the increment of shear strain $\Delta\gamma_{12}$, and (d) the solid fraction ϕ against the increment of shear strain $\Delta\gamma_{12}$. The quantity ϕ does not exist in the original model, and hence only the new model is shown in subfigure (d).

Figure 9 shows that in the original model, the stress paths of τ_{12}, p and q diverge as $\bar{\omega}$ varies, while in the new model, they converge to similar values. As for the constant volume system, this behaviour may be attributed to the different critical states of the two models, with the new model able to approach its critical state at any value of B, while the original model can only do so as $B \to 1$. The system with $\bar{\omega} = 90°$ experiences no breakage and so finds a steady state where the underlying state variables no longer evolve (notwithstanding that plastic volumetric strains continue to accumulate, so the system is not in the critical state). In comparison to the constant volume loading condition, we note that both models produce more grain breakage, but the difference is more significant in the new model, which also experiences a substantial increase in the solid fraction of the system, demonstrating the more efficient grain packing that occurs as the grain size distribution becomes finer. Further variables of interest from these simulations are shown in supporting information Figure S.2.

We also examine the localisation behaviour of the system in Figure 10, using the methodology that is detailed in supporting information §2. To briefly summarise, we perturb the displacement and micro-rotation fields and observe whether those perturbations grow or decay in time. We find the fastest growing wavelength (if such a wavelength exists) of the perturbation and take that to be twice the width of the shear band. We also evaluate the eigenvalues of the acoustic tensor to determine whether the shear band is compacting or dilating. We truncate the analysis to a shear strain increment of 0.065 as the linear stability analysis is only strictly valid up to the moment of localisation. Beyond this point, it can give only an indication of possible behaviour.

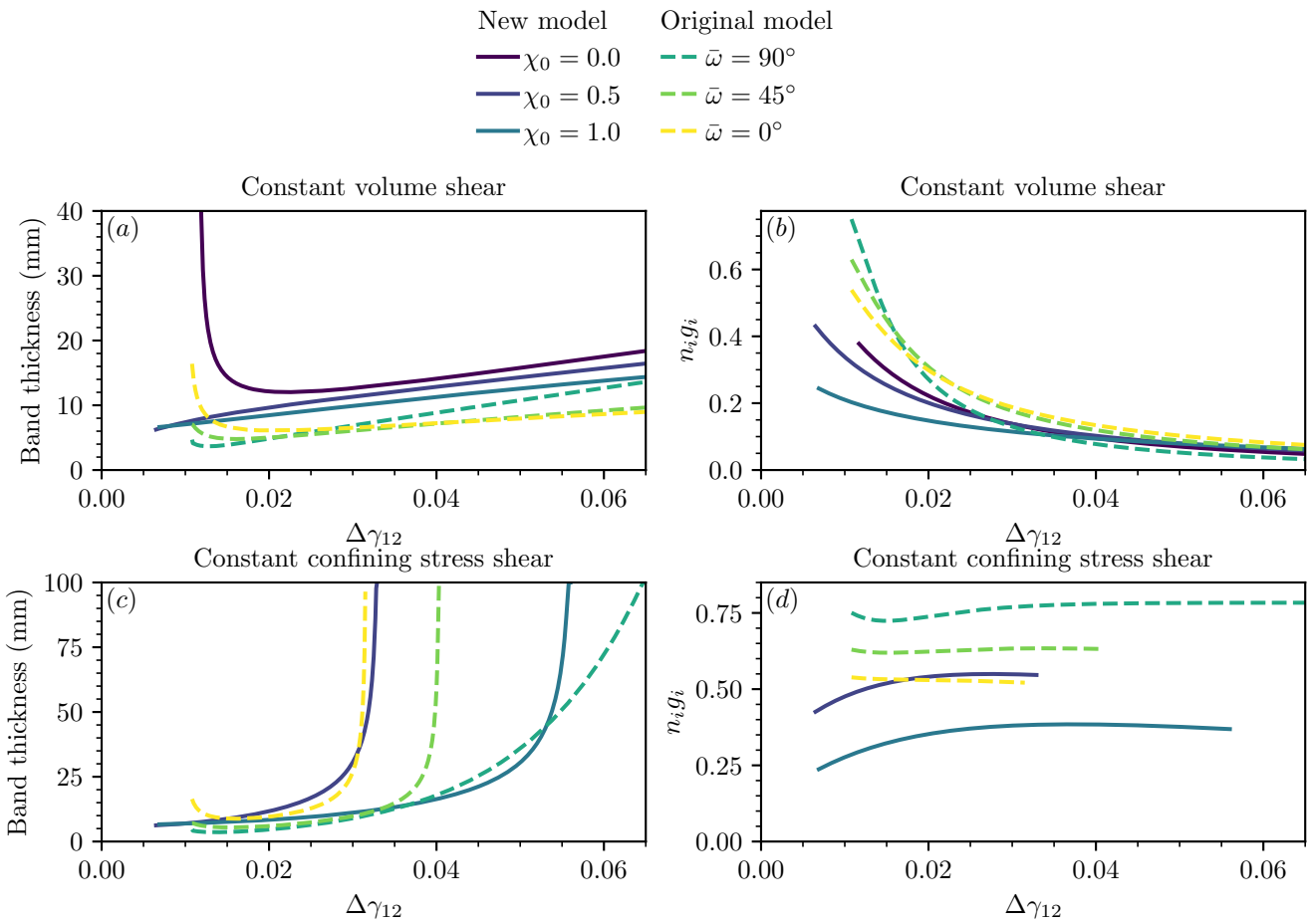

Figure 10: The results of the localisation analysis of simulations of shearing using the model presented in this paper ($\chi \in \{0.0, 0.5, 1.0\}$) and the model presented in Collins-Craft et al. (2020) ($\bar{\omega} \in \{0°, 45°, 90°\}$). (a) The predicted band thickness against the increment of shear strain $\Delta\gamma_{12}$ for shear at constant volume, (b) the product of the orientation of the shear band with the eigenvector associated with the zero eigenvalue of the acoustic tensor against the increment of shear strain $\Delta\gamma_{12}$ for shear at constant volume, (c) the predicted band thickness against the increment of shear strain $\Delta\gamma_{12}$ for shear at constant confining stress, and (d) the product of the orientation of the shear band with the eigenvector associated with the zero eigenvalue of the acoustic tensor against the increment of shear strain $\Delta\gamma_{12}$ for shear at constant confining stress.

Figure 10 shows that in both load conditions the original model typically requires more shear in order to induce a localisation, and that the initial localisation prediction is followed by a rapid decline, and then growth. The new model by contrast demonstrates monotonic growth for all simulations except a relative solid fraction of $\chi_0 = 0.0$ under constant volume, which demonstrates an initial wide localisation that rapidly declines in width before steadily widening again. Notably, in the new model, we observe that the dependence of the initial localisation width on the initial solid fraction ϕ_0 seems to be non-monotonic in the constant volume load condition. To our knowledge, the variation of the shear band width with the solid fraction has not been systematically studied experimentally, but in Alshibli and Sture (2000) the inclination angle of shear bands in biaxial compression tests of sands did not vary monotonically with sample density, particularly at higher confining stress. We take these results to be in alignment with the proposed model prediction that ϕ does not play a strong role in initial shear band thickness, nor is there any particular guarantee of monotonicity between ϕ and the band thickness. The original model displays a greater initial tendency towards compaction in the shear band, but under constant volume conditions all systems trend steadily towards states of pure shear. The systems that favour grain breakage show less tendency towards compaction, with the difference being especially marked for the new model, where the $\chi_0 = 1.0$ system shows only a very light compactive tendency initially. The key difference between the two load conditions is that while the constant volume system delocalises slowly, the constant confining stress condition shows a period of steady growth before delocalising very rapidly. The amount of shear required to delocalise varies with the relative solid fraction, with denser systems requiring greater deformation. The original model produces bands that narrow further and then demonstrate the same tendency to slow growth followed by rapid delocalisation. Both models demonstrate tendency towards plastic compaction under this loading, with the original model showing a substantially stronger effect, as in the constant volume shearing load cases. However, for the range of shear strain in which the shear bands are predicted to exist, there does not appear to be any convergence towards a constant value, unlike in the constant volume case. While experimental measurements

of band thicknesses in conditions equivalent to our own do not exist (to our knowledge), the thicknesses of the initial localisations with respect to the constituent grain sizes (on the order of 10 grain sizes) are coherent with experimental observations made in other test geometries (Mühlhaus and Vardoulakis, 1987; Hall et al., 2010; Andò et al., 2012).

4.3.2 Sensitivity to p

We may also consider the effect of varying p_0, the initial confining pressure, on individual simulations. This represents changes in the burial depth of the fault. We show the load paths of the new model varying p_0 under constant volume shearing in Figure 11.

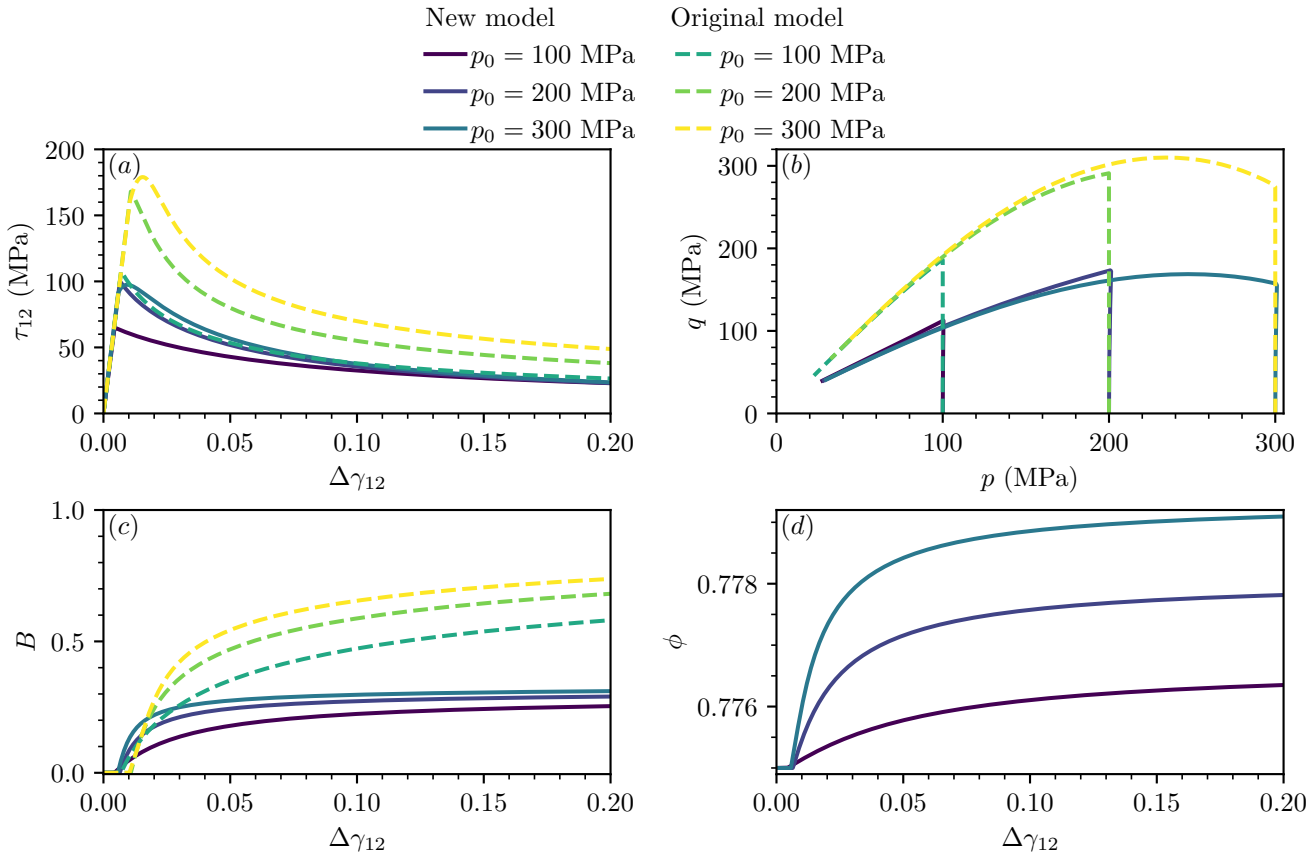

Figure 11: The results of simulations of shearing at constant volume, using the model presented in this paper and the model presented in Collins-Craft et al. (2020) (both with $p_0 \in \{100, 200, 300\}$ MPa). (a) The shear stress τ_{12} against the increment of shear strain $\Delta\gamma_{12}$, (b) the deviatoric stress invariant q against the mean stress p, (c) the breakage index B against the increment of shear strain $\Delta\gamma_{12}$, and (d) the solid fraction ϕ against the increment of shear strain $\Delta\gamma_{12}$. The quantity ϕ does not exist in the original model, and hence only the new model is shown in subfigure (d).

Figure 11 shows that changes to the value of p_0 result in only modest changes to the quantitative behaviour of the system, with qualitative behaviour remaining very similar in this load case. In all cases, the systems demonstrate an apparent softening and an increase in B, with the apparent softening and value of B both being greater with increases in initial confining pressure. The new model demonstrates much less breakage growth than the original model in this system, and the final value of B shows relatively little sensitivity to the initial confining pressure p_0, and the solid fraction increases only slightly. The original model demonstrates much greater rates of breakage growth, accompanied by more dramatic apparent softening. For both models, the system with the highest initial confining pressure ($p_0 = 300$ MPa) shows some post-yield hardening before softening. Further variables of interest from these simulations are shown in supporting information Figure S.3.

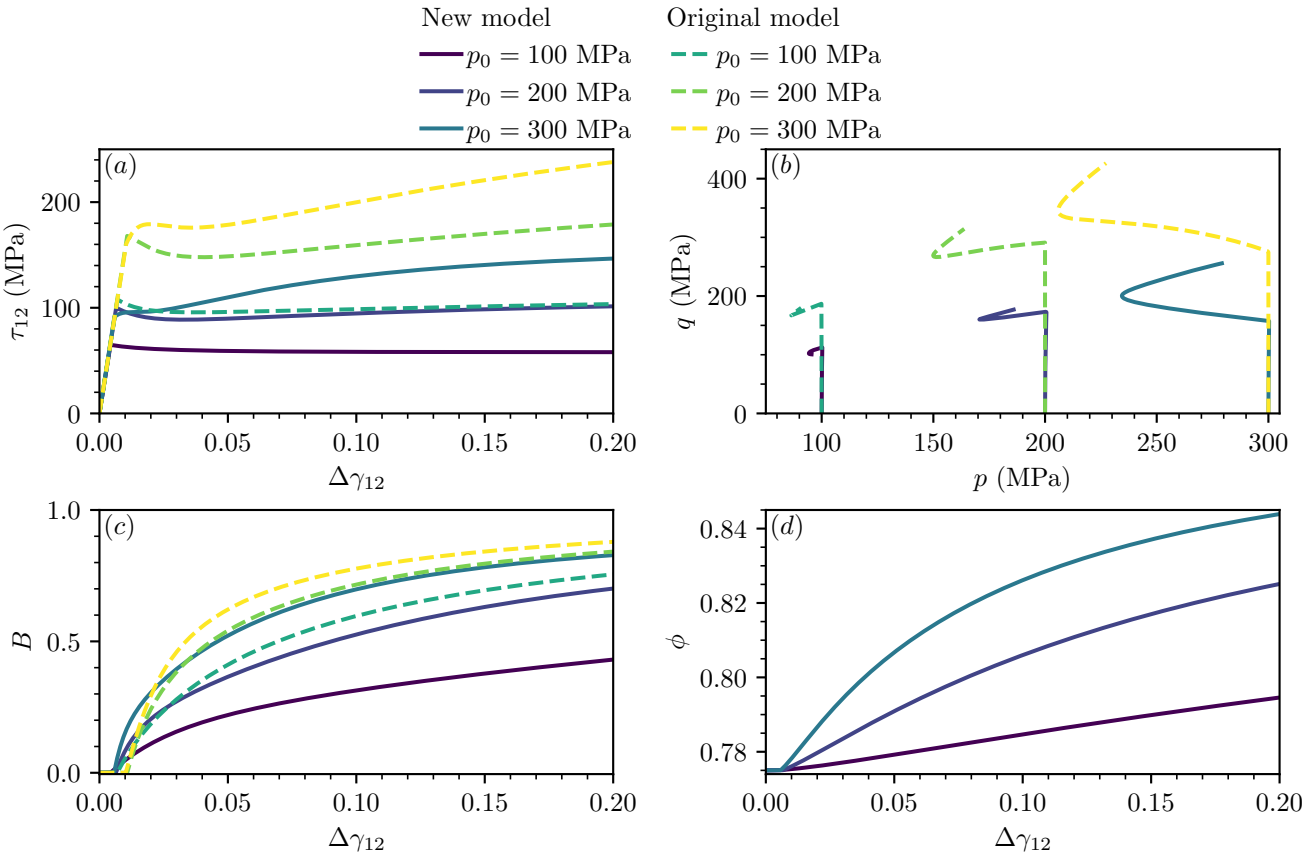

Figure 12: The results of simulations of shearing at constant confining stress, using the model presented in this paper and the model presented in Collins-Craft et al. (2020) (both with $p_0 \in \{100, 200, 300\}$ MPa). (a) The shear stress τ_{12} against the increment of shear strain $\Delta\gamma_{12}$, (b) the deviatoric stress invariant q against the mean stress p, (c) the breakage index B against the increment of shear strain $\Delta\gamma_{12}$, and (d) the solid fraction ϕ against the increment of shear strain $\Delta\gamma_{12}$. The quantity ϕ does not exist in the original model, and hence only the new model is shown in subfigure (d).

Figure 12 shows that under constant confining pressure changing the value of p_0 can result in notable qualitative changes to the system, in contrast to the behaviour under constant volume shearing. For the original model, all systems demonstrate rapid growth in the value of the breakage index B, initial decreases in the value of p followed by increases, and strong initial compactive tendencies that then move towards a state of pure shear. While the values of q in the original model initially show some apparent softening for the lower initial confining stress simulations, they ultimately begin increasing again, while for the system under the greatest initial confining stress, this increase is monotonic. For the new model, we observe that the evolution of the system is slower than for the original model in all cases, with smaller (although still significant) increases in the value of B, as well as significant densification. While the system with the highest initial confining stress follows a qualitatively similar trajectory to the original model, the system at the lowest initial confining stress demonstrates a continuous slow decline in the value of τ_{12}, and the trajectory in the $p - q$ plane changes very little. This indicates that the system is close to the critical state. This qualitative difference in behaviour can only be achieved with the more realistic representation of the critical state in the new model. Further variables of interest from these simulations are shown in supporting information Figure S.4.

We examine the changes in the system's localisation behaviour as the initial confining pressure p_0 is varied in Figure 13.

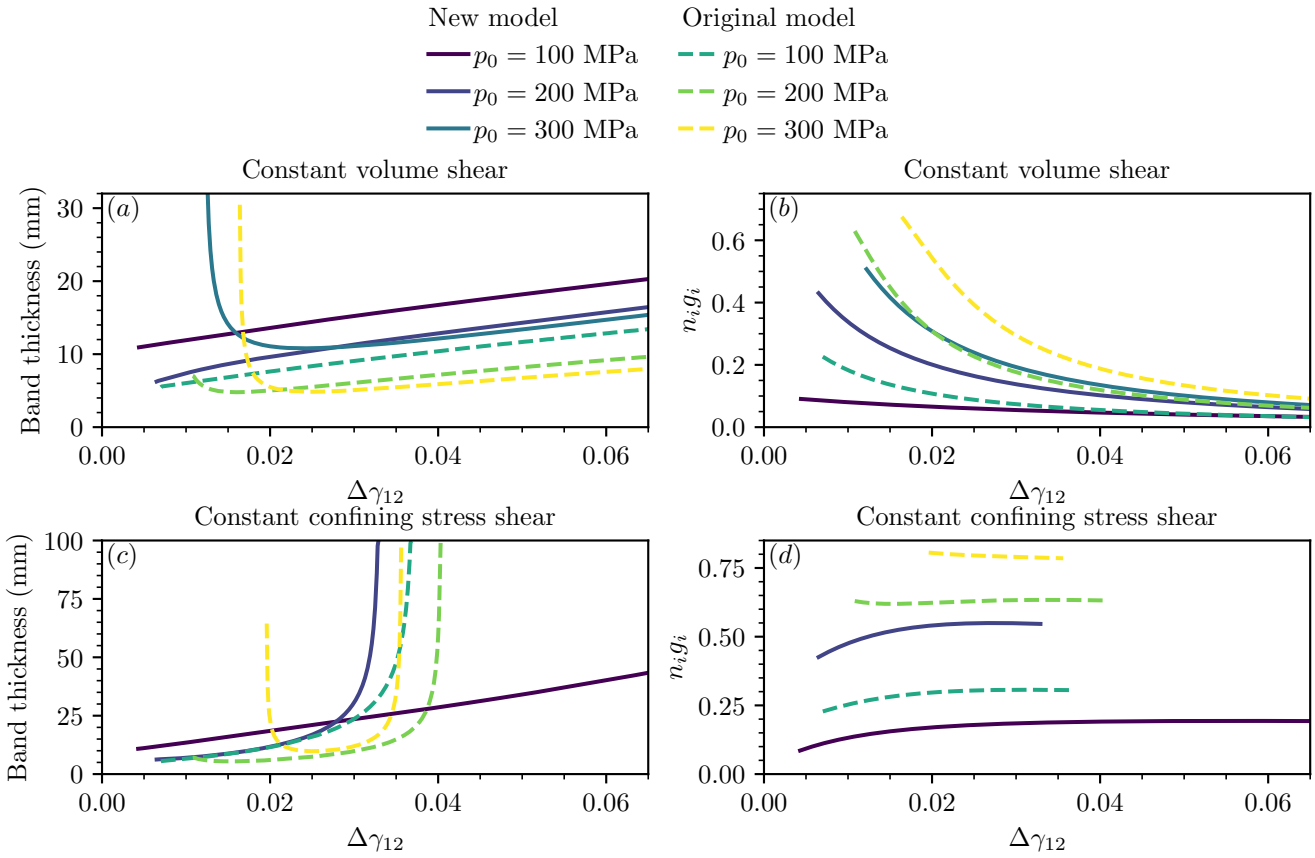

Figure 13: The results of the localisation analysis of simulations of shearing, using the model presented in this paper and the model presented in Collins-Craft et al. (2020) (both with $p_0 \in \{100, 200, 300\}$ MPa). (a) The predicted band thickness against the increment of shear strain $\Delta\gamma_{12}$ for shear at constant volume, (b) the product of the orientation of the shear band with the eigenvector associated with the zero eigenvalue of the acoustic tensor against the increment of shear strain $\Delta\gamma_{12}$ for shear at constant volume, (c) the predicted band thickness against the increment of shear strain $\Delta\gamma_{12}$ for shear at constant confining stress, and (d) the product of the orientation of the shear band with the eigenvector associated with the zero eigenvalue of the acoustic tensor against the increment of shear strain $\Delta\gamma_{12}$ for shear at constant confining stress.

In Figure 13 for both load cases the initial localisation behaviour depends strongly on the initial confining pressure. In constant volume conditions, the higher the initial confining pressure p_0, the more shearing is required to induce a localisation, and initial localisations are wider for higher confining pressure. However, as shear continues, the more strongly confined systems produce narrower shear bands. The constant confining stress systems in the original model all show an initial localisation, then a period of steady increase in width, before rapidly delocalising. In the new model the highest confining stress system ($p_0 = 300$ MPa) does not localise, and the lowest confining stress system ($p_0 = 100$ MPa), grows steadily in width rather than rapidly delocalising. The intermediate system exhibits the same pattern of behaviour as the original model. Once again, all systems indicate that they support a compacting shear band, with the systems all evolving towards pure shear bands in the case of shearing under constant volume (noting that in the new model the least-confined system is very close to pure shear from the start of the localisation). In the constant confining stress case, the systems all indicate compacting shear bands, with the degree of compaction increasing monotonically with the confining stress. Once again, we observe that the size of the shear band relative to the characteristic grain size is coherent with experimental observations, albeit obtained in other geometries (Mühlhaus and Vardoulakis, 1987; Hall et al., 2010; Andò et al., 2012).

4.4 Finite element simulations

Formally, the linear stability analysis is only valid up until the moment of localisation, as an assumption of the analysis is a bifurcation from a homogeneous to a non-homogeneous state of deformation. Thus, the trends observed after this point can at best be taken as indicative of the overall behaviour. In order to obtain a more exact analysis of the post-localisation behaviour, we use instead a method that does not require any assumption of homogeneity, namely the finite element method. We set up the finite element simulations as described in supporting information §5 based on the Numerical Geolab framework (Stefanou and Stathas, 2023), and consider the same variation in the loading conditions as well as χ_0 and p_0 as for the linear stability analysis. All systems have zero horizontal and vertical displacements and

micro-rotations fixed on the bottom of the system and sufficient horizontal displacement on the top boundary to cause a homogeneous strain of 0.2, with the appropriate initial isotropic confining stress applied throughout. The constant volume simulations have zero vertical displacement fixed at the top while the constant confining stress simulations have a constant vertical stress applied. In both cases, the micro-rotations at the top boundary are fixed to zero, so as to recover the classical continuum in the "far-field" limit well away from the shear band. This replicates typical boundary conditions in experimental apparatuses, but couple-stresses at the boundary can be obtained experimentally by shearing using an interface with rough teeth and the ortho-fibre concept (Froiio et al., 2010; Froiio and Zervos, 2019; Vardoulakis, 2019).

We construct spatiotemporal plots of the evolution of the key variables to demonstrate the qualitative behaviour in Figure 14.

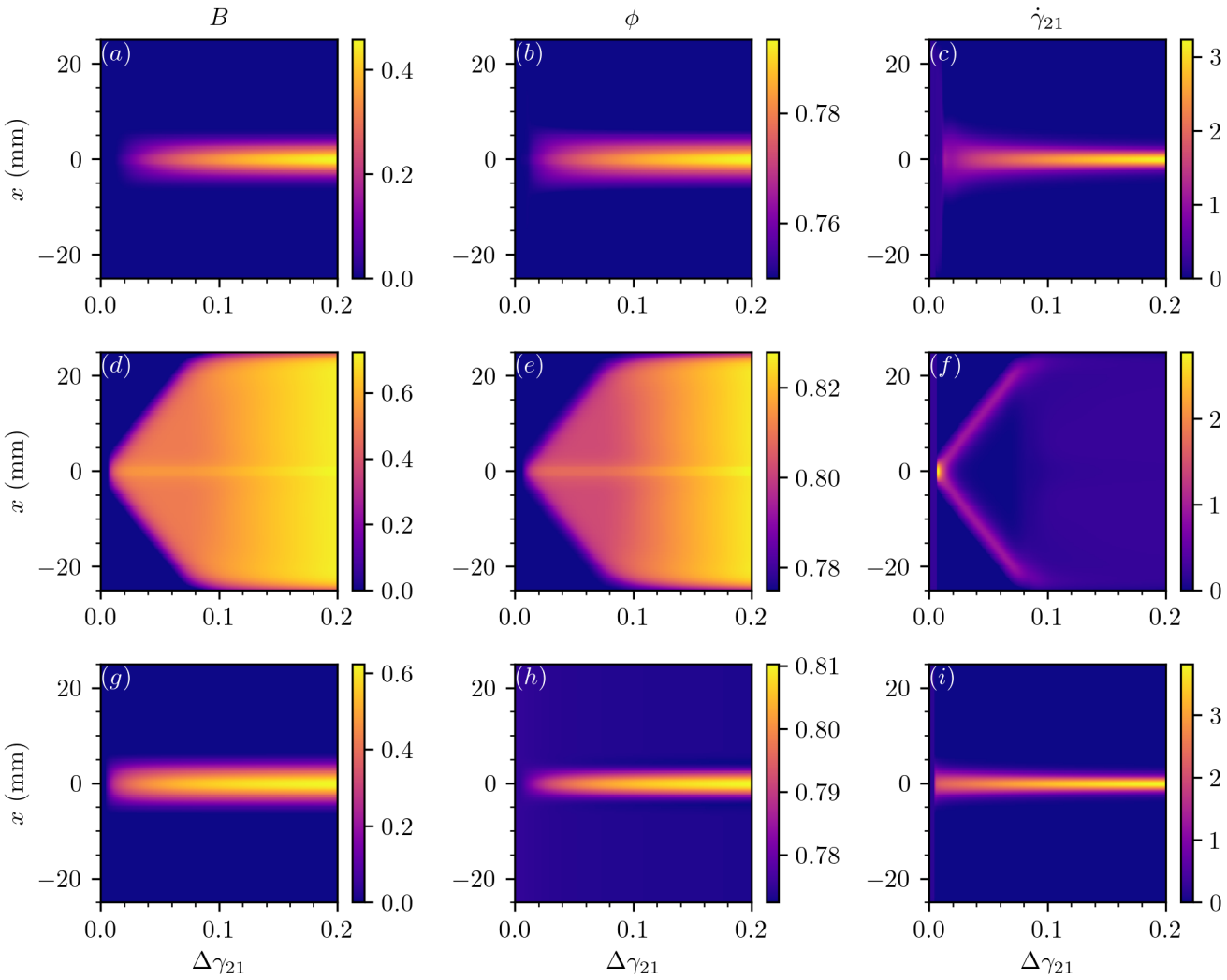

Figure 14: Spatiotemporal plots of three finite element simulations. The first column (subfigures (a), (d), (g)) are the values of B, the second column (subfigures (b), (e), (h)) are the values of ϕ while the third column (subfigures (c), (f), (i)) are the values of $\dot{\gamma}_{21}$. The first row (subfigures (a), (b), (c)) represent the constant volume simulation with $\chi_0 = 0.0$ and $p_0 = 200$ MPa, the second row (subfigures (d), (e), (f)) the constant confining stress simulation with $\chi_0 = 0.5$ and $p_0 = 200$ MPa and the third row (subfigures (g), (h), (i)) the constant volume simulation with $p_0 = 100$ MPa and $\chi_0 = 0.5$.

In Figure 14, we show the results of three simulations that represent the three classes of behaviour that can be observed over the full variation of p_0, χ_0 and the loading conditions. The first class (shown in the first row of subfigures) is localisation into a relatively homogeneous band width where the rate of shear straining shows an increasing concentration at the centre of the band, suggesting a transition from continuous to discontinuous bifurcation of the system (Rice and Rudnicki, 1980), where all deformation is accommodated in the band and elastic unloading outside the band becomes possible. The second class (shown in the second row of subfigures) is localisation into a shear band that then begins to delocalise. Here we can see that the shear strain rate decreases dramatically in the centre of the band and two zones featuring the most intense shearing move outwards from the centre until reaching

the boundary. At the point at which the influence of the boundaries becomes significant, the system shears in a near-homogeneous fashion accompanied by steady GSD changes and densification throughout. The third class (shown in the third row of subfigures) is localisation into a band featuring increasing grain breakage and densification (similar to the first class), but accompanied by the formation of regions of dilation outside the band.

4.5 Comparison of band thickness predictions from linear stability analyses and finite element simulations

We compare the predictions of the LSA against the results of the FEM analyses with respect to the initial band thickness in Figure 15, where we have conducted additional simulations with relative solid fraction $\chi_0 \in \{0.25, 0.75\}$ and initial confining pressure $p_0 \in \{150, 250\}$ MPa to gain a clearer understanding of the variation of the system with the problem parameters.

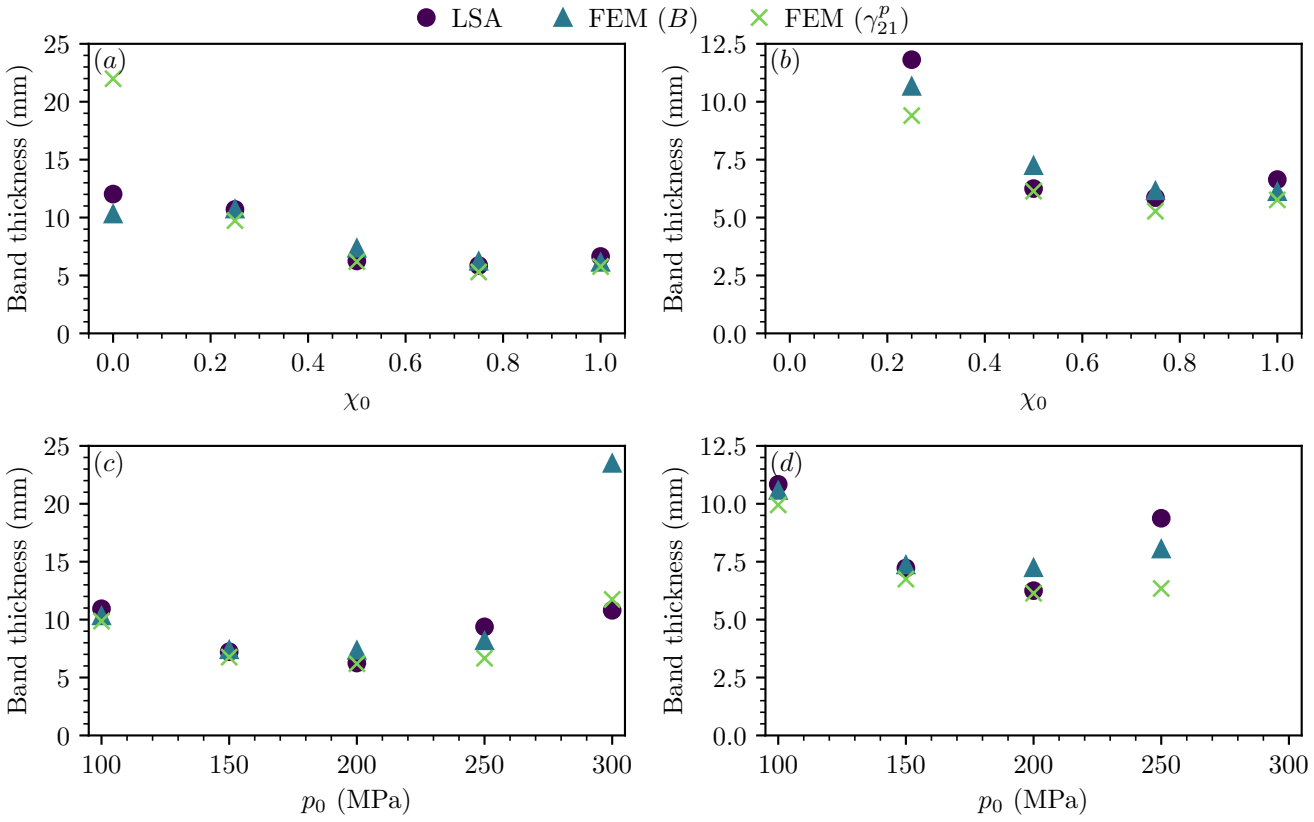

Figure 15: The predicted shear band widths from the LSA, and those inferred from the FEM simulations based on fitting on the spatial distribution of B and γ^p_{21}. For systems where the LSA predicts an initially very wide shear bands that rapidly narrows, we take the minimum band width as the representative value. For the finite element simulations, we take the first values at which the band width stabilises (*i.e.* where it isn't unduly influenced by the initial imperfection). (a) The initial shear band widths when shearing under constant volume and varying χ_0, (b) the initial shear band widths when shearing under constant confining stress and varying χ_0, (c) the initial shear band widths when shearing under constant volume and varying p_0, and (d) the initial shear band widths when shearing under constant confining stress and varying p_0.

We observe in Figure 15 that the LSA predictions generally correspond very well to the width of the shear band in the FEM simulations inferred by the technique in Appendix B. The only visible exceptions are the width inferred by fitting over γ^p_{21} when χ_0 is equal to zero, and the width inferred by fitting over B when $p_0 = 300$ MPa. In both cases, the fitting overestimates the width of the band due to the influence of initial near-homogeneous growth in those values prior to truly localising. Changing the initial solid fraction of the system χ_0 does not lead to substantially different initial shear band widths, in either constant volume or constant confining stress systems. We observe that the finite element fittings with γ^p_{21} also demonstrate the same nonmonotonicity with χ_0 as the results from the linear stability analyses that is observed in both load conditions. Similarly, we observe that changing the initial confining pressure also does not induce dramatically different band widths, and the relationship between the initial confining pressure and the shear band width is nonmonotonic. Both the LSA results and FEM fittings capture these trends, and there is very close agreement in the predicted widths obtained with each method.

4.6 Permeability reduction

Beyond the purely mechanical behaviour, the spatially complex evolution of the state variables captured in the finite element simulations also influence the permeability of the system to fluids. We can calculate the ratio of the current permeability at a point to its original permeability using (75).

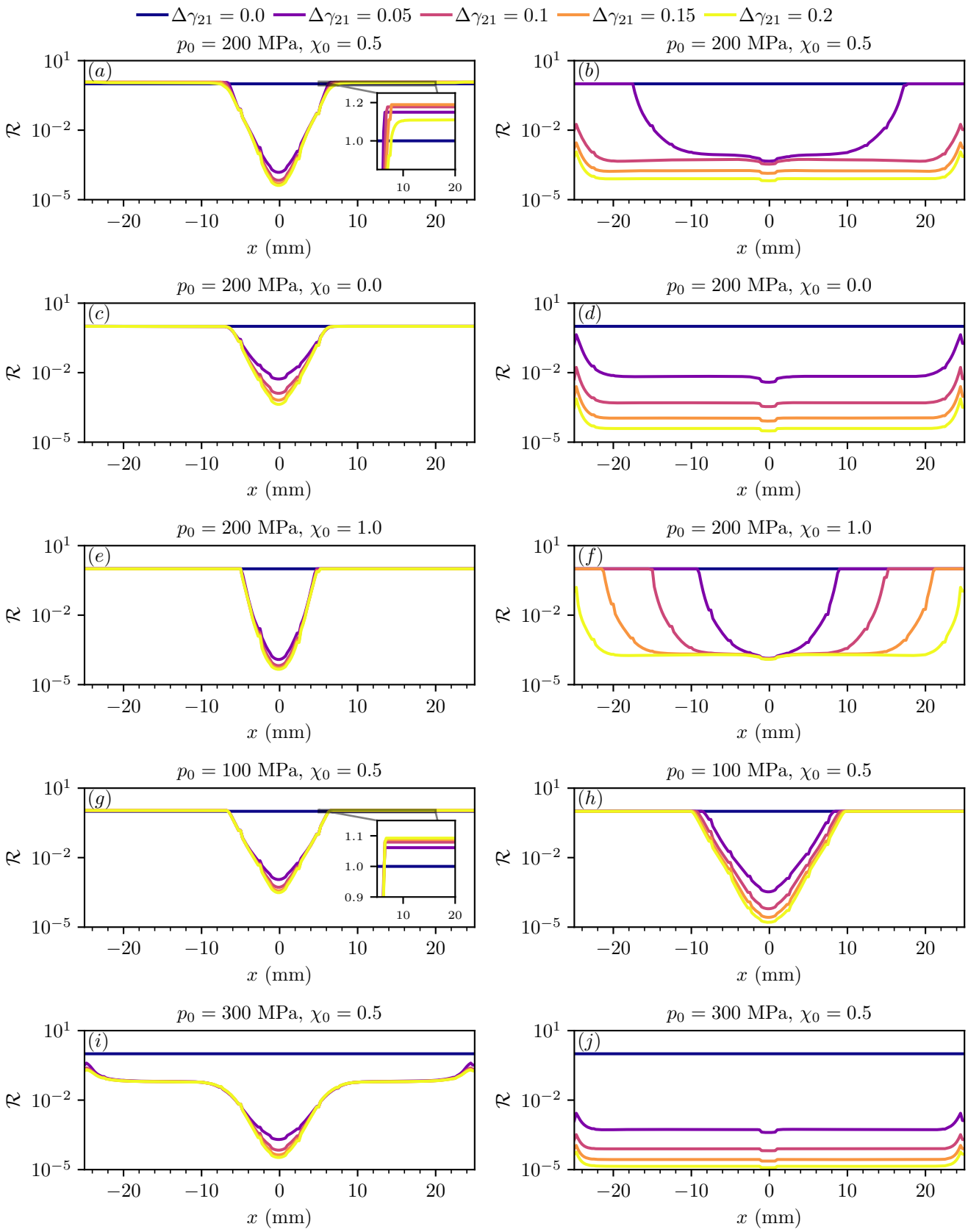

Figure 16: The ratio of the current permeability to the original permeability, for a selection of finite element system simulated, at a selection of key strain increments. The first column of subfigures ((a), (c), (e), (g), (i)) are the simulations under constant volume, while the second column of subfigures ((b), (d), (f), (h), (j)) are the simulations under constant confining stress. The insets in subfigures (a) and (g) show the permeability ratio in the region defined by the x-coordinate 5 to 20, with ratios less than 0.9 not shown.

Figure 16 demonstrates the very large differences in permeability evolution between the simulations under constant volume and under constant confining stress. The general trend of the constant confining stress simulations (those in

the right-hand column of Figure 16) is to have a relatively homogeneous decrease in the permeability ratio across the system, other than where the effect of the boundaries becomes significant. The exception to this is the system that is slowest to delocalise, that with $p_0 = 100$ MPa. Due to the greater concentration of shearing at the centre of the band thanks to the absence of complete delocalisation, this system induces more grain crushing and porosity reduction at its centre, causing in turn larger decreases in the permeability than are observed for systems with initial conditions that are (notionally) more favourable to grain crushing and pore collapse. Turning to the systems sheared under constant volume (those in the left-hand column of Figure 16), we observe that in general the systems that favour grain breakage over pore collapse (higher initial values of χ_0) are those that feature the greatest reductions in permeability ratio, indicating that within the proposed model the increase in tortuosity induced by the presence of large numbers of small grains plays a more important role than the reduction in pore space when it comes to reducing the permeability ratio. Of particular interest for the constant volume loading case is the changes induced outside the shear band. For the system with $\chi_0 = 0.5$ and $p_0 = 200$ MPa, we observe changes that depend on the amount of shearing applied to the system. For low to moderate values of homogeneous shear straining, we see that the dilation that occurs outside the band leads to increases in the permeability ratio, facilitating fluid flow. However, after a certain point small amounts of breakage are induced which reverses this trend, and we see a small reduction in permeability outside the band (relative to the peak permeability values, however the permeability remains greater than its initial value). Finally, for the system with $p_0 = 100$ MPa, we observe that increasing the shear strain monotonically increases the permeability outside the band due to dilation.

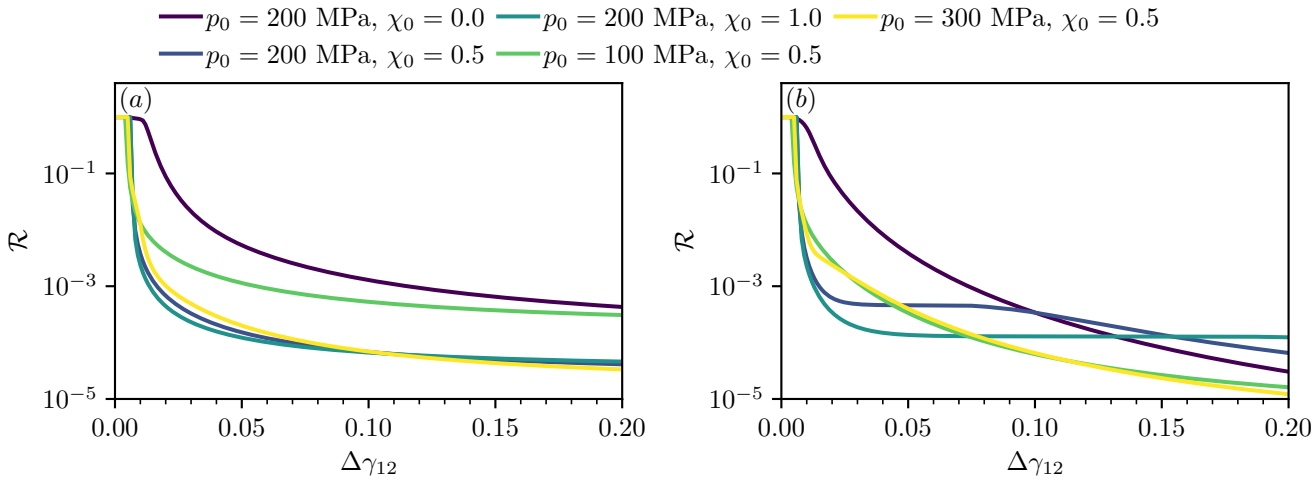

Figure 17: The permeability ratio at the centre of the band against the homogeneous shear strain for the systems sheared under (a) constant volume and (b) constant confining stress.

In Figure 17 we may observe the evolution of the minimum value of the permeability ratio in the system against the homogeneous shear strain. For both systems we observe that changing the initial relative solid fraction χ_0 and increasing the initial confining pressure p_0 typically favour greater reductions in the permeability ratio. The constant volume systems demonstrate a relatively constant shape, with fast initial reductions in permeability ratio followed by much longer periods of smaller but steady decline. While two of the constant confining stress systems show this same pattern (notably, the two systems that either do not delocalise during the simulation or do not localise at all), the three other systems show "kinks" as the rate of permeability reduction decreases substantially before plateauing or beginning to decline at steady rates. This behaviour is linked to the structural evolution of the band as it delocalises, with plateaus in the permeability ratio being linked to the shearing (and hence evolution of B and ϕ) largely occurring at the edges of the band, rather than in the centre. For the systems where the band reaches the edge of the system, the evolution proceeds quasi-homogeneously, with the only variations due to the boundaries and the initial imperfection. Hence, the centre resumes its evolution. As the $\chi_0 = 1.0$ system only just completes its delocalisation over the course of the simulation, the system is still evolving towards the quasi-homogeneous evolution by accumulating breakage and porosity reduction at the boundaries, and so no meaningful evolution of the permeability ratio at the centre occurs. We note that under constant confining stress, after the $p_0 = 300$ MPa system has completed its delocalisation, there is very little difference between its permeability ratio and that of the $p_0 = 100$ MPa system, demonstrating that the continued concentration of shearing at the centre of the band for the latter system is able to drive similar amounts of grain crushing and pore collapse as the greater confining stress induces with more diffused shearing.

5 Discussion

5.1 Physical accuracy of the model

We have shown in §4.3 and §4.4 that changing the model parameters and state variables changes the physical characteristics of the system by modifying the way in which the compaction and grain crushing coevolve and potentially compete with dilation. This includes the shape of the resulting yield surface, where the model can accommodate cohesion c that depends on the extent of the grain crushing B, classical convex yield surfaces that are able to capture the increasing amount of energy required to crush grains as compaction continues, as well as non-convex yield surfaces that arise in the proposed model as a consequence of dilation and reductions in the solid fraction ϕ at lower confining stresses. This last factor allows for a substantially better match to experimental data on Bentheim sandstones than was possible with the model that we developed in Collins-Craft et al. (2020). Once the model experiences plasticity, changes in these material parameters are able to account for markedly different behaviours immediately post-yield, while also capturing the tendency of the systems to evolve towards similar states, whereas the previously developed model features trajectories that vary substantially as the parameter values are changed, even though the initial state variables are the same. This again highlights the superior physical accuracy of the model developed in this paper, as it respects the observed tendency of soils and rocks to converge to similar stress ratios under continued loading, even if the initial behaviour is substantially different (Lade and Bopp, 2005; Bandini and Coop, 2011).

While in this paper we have focused on the modelling of a large-grained and porous sandstone, the formalism is suitable for other types of minerals and can be applied to any sort of rock featuring distinct and crushable grains such as limestones (Abdallah et al., 2021; Doré-Ossipyan et al., 2025).

5.2 Discrepancies between the predictions of the linear stability analysis and the finite element simulations

In the constant volume load case the LSA predicted gradual delocalisation while the inferred shear band widths from the FEM analyses remain stable. By contrast, the post-localisation behaviour under constant confining stress in the FEM simulations corresponds very well with the predictions of the LSA. The shear band rapidly delocalises, as the LSA predicted, and the speed of this delocalisation depends strongly on the values of χ_0 and p_0, as predicted. The only meaningful difference between the LSA predictions and the results of the FEM simulations are for the $\chi_0 = 1.0$ and $p_0 = 100$ MPa systems, which delocalise more slowly than the LSA predicts, and the interaction with the boundaries of the system that occurs for the most rapidly delocalising systems. We may observe that the underlying reason for the interaction with the boundaries is that the shear bands under this loading condition concentrate their strain rate at the boundaries of the band, which march steadily outwards. This behaviour is illustrated in Figure 18.

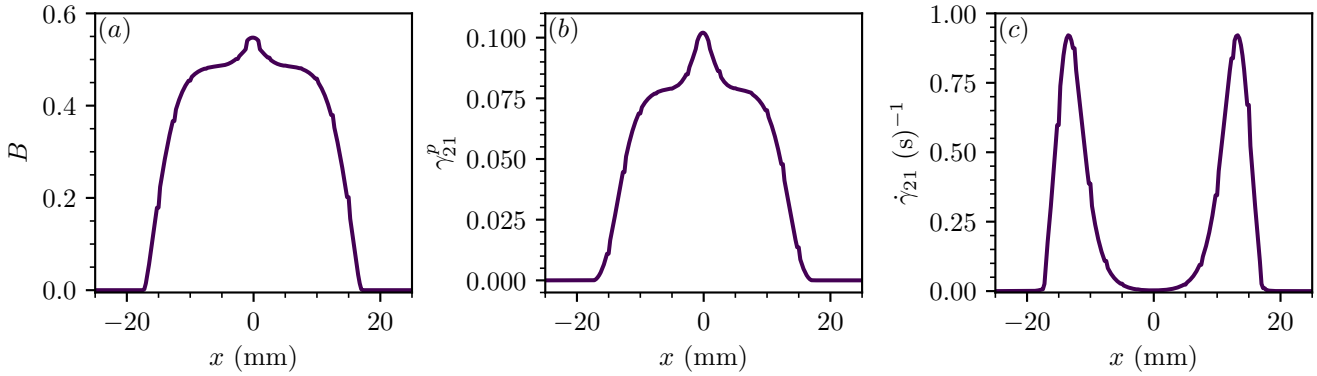

Figure 18: The spatial distributions of the some key variables at homogeneous shear strain $\Delta\gamma_{21} = 0.05$ for the simulation with $\chi_0 = 0.5$ under constant confining stress (a) The spatial distribution of B, (b) the spatial distribution of γ_{21}^p, and (c) the spatial distribution of $\dot{\gamma}_{21}$.

Figure 18 demonstrates clearly that while the shear band continues growing in the centre, the shearing occurs preferentially at the edges of the band, causing it to grow outwards until the boundary conditions interfere with further propagation.

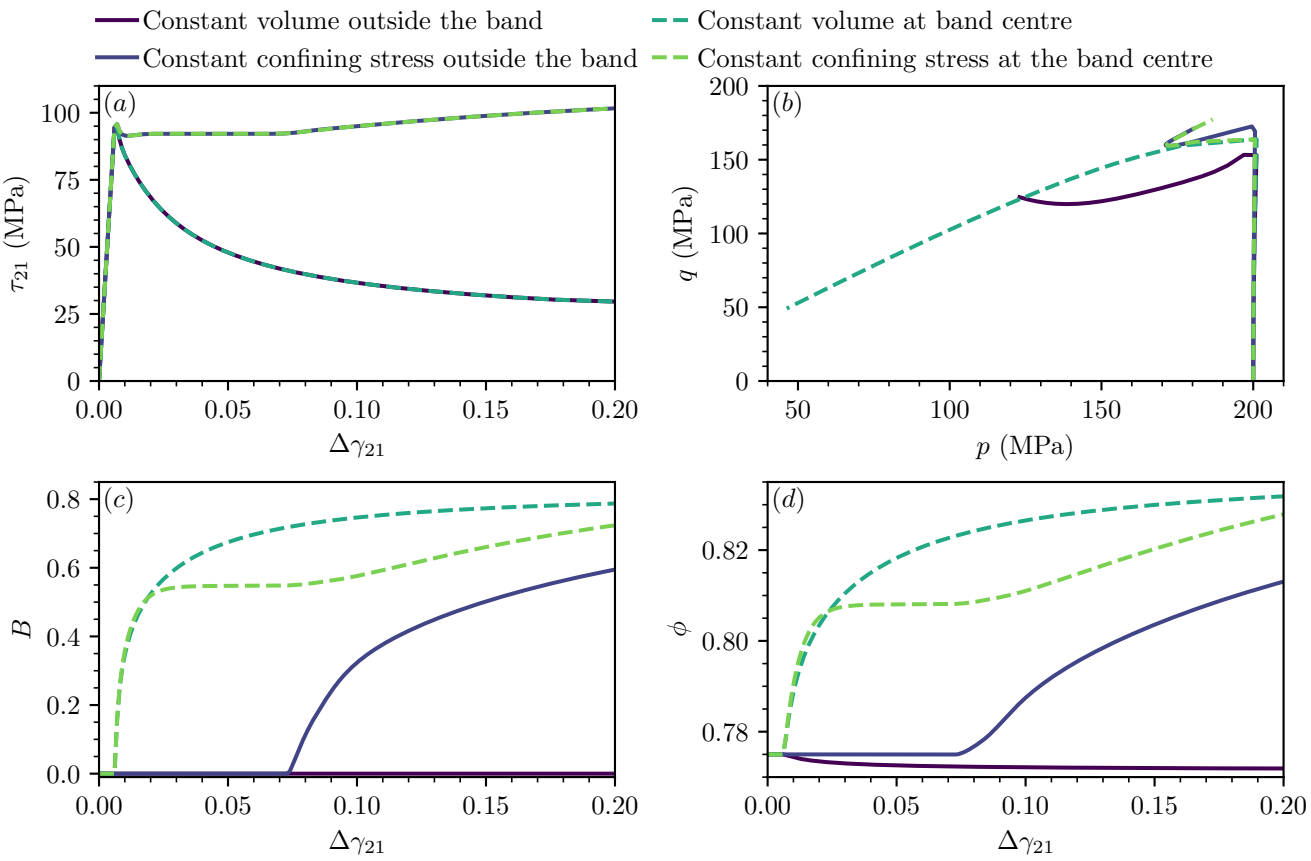

Figure 19: The results of simulations of shearing at constant volume and constant confining stress with $\chi_0 = 0.5$ and an initial confining stress of 200 MPa, considering points either near the edge of the system or at the centre of the band. (a) The shear stress τ_{21} against the increment of (homogeneous) shear strain $\Delta\gamma_{21}$, (b) the deviatoric stress invariant q against the mean stress p, (c) the breakage index B against the increment of shear strain $\Delta\gamma_{21}$, and (d) the solid fraction ϕ against the increment of (homogeneous) shear strain $\Delta\gamma_{21}$.

In Figure 19 we examine the different evolutions of the state variables inside and outside the shear band, taking the central values of $\chi_0 = 0.5$ and $p_0 = 200$ MPa as representative of the general behaviours. The values at the centre of the shear band are those for the elements with the highest value of B at the end of the simulation, while the values outside the band are taken to be the values five elements in from the top of the system, to avoid distortions from the boundary. As expected, τ_{12} matches perfectly due to the need to maintain stress equilibrium, while p and q show similar tendencies inside and outside the band for the constant confining stress system, but vary somewhat for the constant volume system. Where the most dramatic differences are observed is in the evolution of the breakage and solid fraction. Here, the local concentration of strain (noting that the amount of strain experienced in this central element is much higher than the global homogeneous strain) drives the breakage higher rapidly. This drives in turn a substantial increase in the solid fraction, both in order to stay within the bounds imposed by (18) and (19), but also to maintain the necessary stress equilibrium, keeping in mind that for a fixed elastic strain, an increase in B will reduce the stress while an increase in ϕ will increase the stress (*via* changing ρ). It is only as the band delocalises for the constant confining stress system that we observe any substantial evolution of these quantities at the point that was (initially) outside the band. The constant volume FEM simulation grows the breakage and solid fraction values slightly faster than the constant confining stress system, due to a greater local concentration of shearing. Outside the band, we observe a slight decrease in ϕ due to elastic dilation. Further variables of interest from these simulations are shown in supporting information Figure S.5.

One of the key differences between the single element tests and the finite element systems is that the finite element method is able to account for structural features that vary in space. The most important spatial variations (other than the localisation into the shear band itself) are the outwards spreading of the shear strain rate observed for the constant confining stress simulations, and the dilation observed for the constant volume tests. These two phenomena cause the band to either experience less shear straining at the centre than would be expected, or permit additional compaction to be accommodated in the band than the boundary conditions allow for single element tests.

5.3 Permeability changes in real rocks

When considering the changes in permeability at the centre of the band shown in Figure 17, it is the $\chi_0 = 1.0$ system that shows the most rapid initial reductions in permeability ratio, under both constant volume and constant confining stress systems. The decrease in permeability in the constant confining stress system then pauses while the band expands outwards. This behaviour indicates that not only are the densest (least porous) systems the ones that are likely to have the lowest initial permeability, but that they are also likely to experience the greatest permeability reduction during the formation of the shear band (notwithstanding that other systems may have lower permeability values in more mature bands as they do not delocalise as strongly). Experimental values for the permeability of Bentheim sandstone are typically in the range of 1–7.5$\times10^{-13}$ m^2 (Vajdova et al., 2004; Fazio et al., 2023), so applying our reductions in permeability ratio, we could expect to see permeability values at the centre of the shear band ranging from 1×10^{-18} to 7.5×10^{-16}, depending on the initial relative solid fraction and the loading conditions applied to the system. The lower part of this permeability range is more typical of claystones than sandstones (Neuzil, 2019), highlighting the dramatic effect of breakage evolution and pore collapse on the hydraulic properties of the material, and further underlining the importance of mechanical models that can account for this effect in the accurate modelling of faults, as such dramatic permeability changes will substantially influence the hydraulic and thermal coupling that governs the behaviour of the system. As the model developed in Collins-Craft et al. (2020) has no representation of the porosity (and plastic volumetric compaction can occur indefinitely in that model, without regard to physical limits), it is unable to represent the permeability in any meaningful way, given the strong dependence on the pore volume of the material.

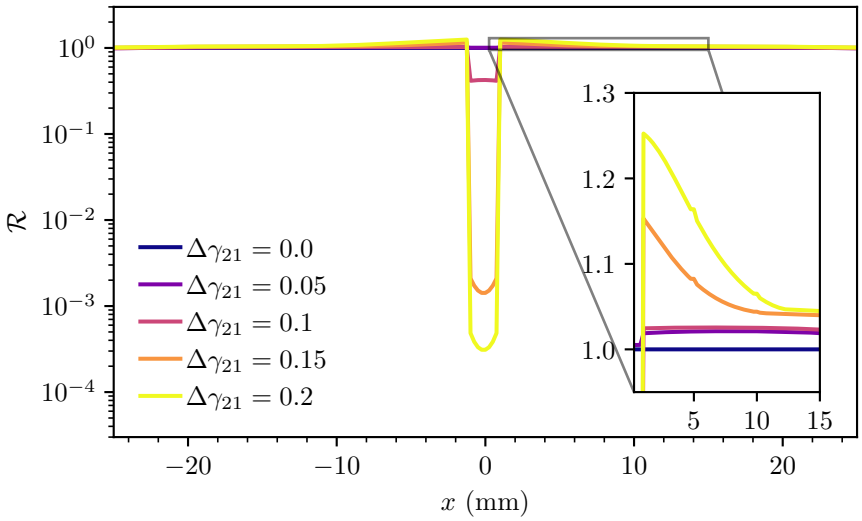

Figure 20: The ratio of the current permeability to the original permeability for the constant volume finite element system with $\zeta = 1$, $\chi_0 = 0.5$ and $p_0 = 100$ MPa, at a selection of key strain increments. The inset shows the permeability ratio in the region defined by the x-coordinate 5 to 17.5, with ratios less than 0.95 not shown.

In Figure 20, we examine the permeability ratio of a system sheared under constant volume using the central parameter value $\chi_0 = 0.5$, a low confining pressure of $p_0 = 100$ MPa, and $\zeta = 1.0$, meaning that the system favours dilation more than the other systems examined in this paper. We observe that in this case, we have a marked increase in the permeability of the system in two bands on either side of the principal shear band, with the permeability increasing more with increasing shearing. For all values of shear strain increment that these bands appear in, the maximal permeability ratio not only increases, but the bands become wider. These numerical results correspond to experimental observations on sands which have shown that even small amounts of grain breakage concentrated in shear bands substantially reduces the permeability (Feia et al., 2016; Benammar et al., 2025). Directional permeability measurements on Bentheim sandstone samples with a shear band featuring grain crushing have demonstrated strong permeability decreases transverse to the shear band, but permeability increases parallel to it (Dautriat et al., 2009). As grain crushing increases the tortuosity (thus reducing the permeability) isotropically, we would expect flow along the cataclastic shear band to also decrease, contrary to the experimental evidence. From these results, we infer the existence of structures favouring flow parallel to the band, an inference that is strengthened by experimental observations on Fontainebleau sandstone, which have shown the presence of dilating zones with increased porosity outside compacting shear bands (El Bied et al., 2002), and that these dilating zones are capable of absorbing pore fluid expelled from the compacting region due to their much higher porosity and permeability (Sulem and Ouffroukh, 2006). Observations in the field, albeit on different types of rocks, have also shown the presence of zones with higher permeability than the host rock that are immediately adjacent to the fault core (Wibberley and Shimamoto, 2003; Micarelli et al., 2006).

5.4 Comparison of the new and original models

In single-point simulations, we observe that the new model generally exhibits slower changes to its underlying state variables, in particular the breakage index B. This occurs as the new model also includes the solid fraction, and as the two variables co-evolve the system typically finds states that lead to ω increasing, and hence the rate of breakage decreasing. By contrast, in the original model, the rate of breakage is meaningfully modified only by the value of B, so it is only as $B \to 1$ that the rate of breakage slows down. As a consequence of this behaviour, the new model offers physically more realistic evolutions of the GSD with increasing strain. Changes in the initial relative solid fraction modify the initial behaviour of the system in a way similar to changing $\bar{\omega}$ in the original model, but the balancing of B and ϕ evolution in the new model causes the systems to tend towards similar states, regardless of the starting position, while the original model can demonstrate extremely divergent behaviour depending on the value of $\bar{\omega}$. We also observe that our new model consistently predicts the appearance of shear bands earlier than the original model, specifically at the initiation of plasticity. While in real geomaterials it is generally not possible to cleanly distinguish when plasticity commences, at the very least we can note that the early localisation of the new model is much closer to observed experimental phenomena in triaxial tests on sand (Desrues et al., 2018), in which shear bands appear well before the peak stress. Our model could easily be adapted to no longer cleanly separate between elastic and plastic behaviours by reframing it in h^2-plasticity (Einav, 2012), although we have elected to remain in a more classical plasticity framework in this paper for reasons of numerical efficiency.

6 Conclusion

In this paper, we developed a constitutive model in the Cosserat Breakage Mechanics framework introduced in Collins-Craft et al. (2020). This model features a number of improvements that increase its physical fidelity, namely density-dependent elasticity and shear strength, the presence of cohesive strength and the inclusion of the solid fraction ϕ as a state variable, enable the modelling of dilation at lower confining stresses, and the coevolution of the grain size distribution with the pore space at higher confining stresses.

This model was then calibrated against experimental data obtained by other authors on Bentheim sandstone, demonstrating the importance of the new model features to being able to accurately calibrate the yield surface to data obtained over the full range of stresses up to to the crushing pressure. A comparison with triaxial compression tests conducted by Klein et al. (2001) was conducted, demonstrating the ability of the model to represent the real behaviour of the Bentheim sandstone. We then conducted sensitivity analyses of the new model and comparisons with the model presented in Collins-Craft et al. (2020) to examine the mechanical behaviour as the initial solid fraction ϕ_0 and the initial confining stress p_0 were varied. These mechanical analyses were accompanied by predictions of the initial localisation behaviour of the model, determined by linear stability analyses. These analyses highlight that localisation of the new model occurs directly upon the start of plasticity and that the resultant shear bands are compactive at confining stresses typical of earthquake nucleation. In the case of constant confining stress, these bands further demonstrate a tendency to delocalise.

The localisation results obtained by linear stability analyses were subsequently confirmed by one-dimensional finite element simulations that showed close matching for the initial localisation width, and in the case of constant confining stress, confirmed the predicted delocalisation behaviour. Under constant volume conditions, similar to the conditions faults experience during fast undrained shearing, certain systems demonstrate not only the presence of compacting shear bands, but regions of dilation immediately outside the band. Using a modified Kozeny–Carman permeability law, we are able to analyse the evolution of the permeability across the system and observe both orders-of-magnitude reduction of the permeability within the shear band, as well as increases in the permeability in the dilating regions outside the band, corresponding to experimental observations made on similar sandstones.

This work has substantially increased the physical fidelity of the Cosserat Breakage Mechanics model family and broadened the range of materials that it is able to accurately model. The inclusion of an additional state variable gives the model the capability to model phenomena that were previously inaccessible, and enables a coupling of the model with hydrological quantities such as pore fluid flow. This work can thus serve as the mechanical component of coupled thermo-hydro-(chemo)-mechanical models that can fully elucidate the formation of the shear bands that make up the core of seismogenic faults.

Acknowledgements

The first author acknowledges the support of the Marie Skłodowska-Curie Actions program under the Horizon Europe research and innovation framework program (Grant agreement ID 101064805 LEMMA). The second author acknowledges the European Research Council's (ERC) support under the European Union's Horizon 2020 research and innovation programme (Grant agreement no. 101087771 INJECT). Views and opinions expressed are however those of

the authors only and do not necessarily reflect those of the European Union or Horizon Europe. Neither the European Union nor the granting authority can be held responsible for them.

Open Research

The code required to run the simulations described in this paper is available in a GitHub repository that has been archived on Software Heritage, or alternatively as a deposit on Zenodo. The data outputs of the codes are also available on Zenodo.

A Model derivation

A.1 Thermodynamic admissibility

We wish to show that the model specified in §3 is thermodynamically admissible (that is, both the internal energy and the dissipation are never negative).

Firstly, we consider the internal energy of the system. Our definitions of B, θ_γ and θ_κ ensure that $B \in [0,1]$, $\theta_\gamma \in [0, \frac{2}{5-\alpha}]$ and $\theta_\kappa \in [0, \frac{4}{7-\alpha}]$ (all positive for typical values of α of $2.5 \sim 2.7$), the maximum grain size $d_{\mathrm{Max}} > 0$, the density $\rho > 0$ (as is the unstressed solid density $\rho_s^\star$), and the tensors C^e_{ijkl} and D^e_{ijkl}, when transformed to two-dimensional matrices, are positive definite (provided physically admissible values of $\bar{K}$ and $\bar{G}$ are chosen), meaning their products with γ^e_{ij} and κ^e_{ij} (when both transformed to one-dimensional vectors) will both be positive. As such, by inspection we can conclude that (26) is always non-negative.

Demonstrating the positiveness of the dissipation is substantially more elaborate. We start by declaring the Clausius–Duhem inequality for an isothermal process in the Cosserat continuum:

$$\mathcal{D} = \tau_{ij}\dot{\gamma}_{ij} + \mu_{ij}\dot{\kappa}_{ij} - \left(\dot{\mathcal{U}} - \mathcal{U}\frac{\dot{\rho}}{\rho}\right) \geq 0, \tag{46}$$

where $\mathcal{U}$ is the internal energy (we add the hat in (26) to distinguish between the *value* of internal energy (without hat) and the *function* that returns its value given the state variables (with hat)) and $\mathcal{D}$ is the dissipation. From (26) we recover the time rate of the internal energy:

$$\dot{\mathcal{U}} = \frac{\partial\hat{\mathcal{U}}}{\partial\gamma^e_{ij}}\dot{\gamma}^e_{ij} + \frac{\partial\hat{\mathcal{U}}}{\partial\kappa^e_{ij}}\dot{\kappa}^e_{ij} + \frac{\partial\hat{\mathcal{U}}}{\partial\rho}\dot{\rho} + \frac{\partial\hat{\mathcal{U}}}{\partial B}\dot{B}. \tag{47}$$

The mass balance equation is given by

$$\dot{\rho} + \rho\dot{u}_{i,i} = 0. \tag{48}$$

This can equivalently be written as

$$\frac{\dot{\rho}}{\rho} = \dot{\gamma}_{ij}\delta_{ij} = \dot{\varepsilon}_v. \tag{49}$$

Now, substituting (47) and (49) back into (46), we obtain:

$$\mathcal{D} = \tau_{ij}\dot{\gamma}_{ij} + \mu_{ij}\dot{\kappa}_{ij} - \left(\frac{\partial\hat{\mathcal{U}}}{\partial\gamma^e_{ij}}\dot{\gamma}^e_{ij} + \frac{\partial\hat{\mathcal{U}}}{\partial\kappa^e_{ij}}\dot{\kappa}^e_{ij} + \frac{\partial\hat{\mathcal{U}}}{\partial\rho}\dot{\rho} + \frac{\partial\hat{\mathcal{U}}}{\partial B}\dot{B} - \mathcal{U}\dot{\gamma}_{ij}\delta_{ij}\right) \geq 0. \tag{50}$$

Then, using the fact that $\dot{\rho} = \rho\dot{\gamma}_{ij}\delta_{ij}$, and substituting (14) and (15) into (50), we get

$$\begin{aligned}
\mathcal{D} &= \tau_{ij}(\dot{\gamma}^e_{ij} + \dot{\gamma}^p_{ij}) + \mu_{ij}(\dot{\kappa}^e_{ij} + \dot{\kappa}^p_{ij}) - \left(\frac{\partial\hat{\mathcal{U}}}{\partial\gamma^e_{ij}}\dot{\gamma}^e_{ij} + \frac{\partial\hat{\mathcal{U}}}{\partial\kappa^e_{ij}}\dot{\kappa}^e_{ij} + \frac{\partial\hat{\mathcal{U}}}{\partial\rho}\rho(\dot{\gamma}^e_{ij} + \dot{\gamma}^p_{ij})\delta_{ij} + \frac{\partial\hat{\mathcal{U}}}{\partial B}\dot{B} - \mathcal{U}(\dot{\gamma}^e_{ij} + \dot{\gamma}^p_{ij})\delta_{ij}\right) \geq 0, \\
&= \left(\tau_{ij} - \frac{\partial\hat{\mathcal{U}}}{\partial\gamma^e_{ij}} - \left(\rho\frac{\partial\hat{\mathcal{U}}}{\partial\rho} - \mathcal{U}\right)\delta_{ij}\right)\dot{\gamma}^e_{ij} + \left(\mu_{ij} - \frac{\partial\hat{\mathcal{U}}}{\partial\kappa^e_{ij}}\right)\dot{\kappa}^e_{ij} + \left(\tau_{ij} - \left(\rho\frac{\partial\hat{\mathcal{U}}}{\partial\rho} - \mathcal{U}\right)\delta_{ij}\right)\dot{\gamma}^p_{ij} \\
&\quad + \mu_{ij}\dot{\kappa}^p_{ij} - \frac{\partial\hat{\mathcal{U}}}{\partial B}\dot{B} \geq 0.
\end{aligned} \tag{51}$$

(51) must hold true for arbitrary values of $\dot{\gamma}^e_{ij}$, $\dot{\kappa}^e_{ij}$, $\dot{\gamma}^p_{ij}$, $\dot{\kappa}^p_{ij}$ and $\dot{B}$. As purely elastic processes with $\dot{\gamma}^p_{ij}$, $\dot{\kappa}^p_{ij}$ and $\dot{B}$ all equal to zero must not dissipate energy, we conclude the terms inside the brackets multiplying $\dot{\gamma}^e_{ij}$ and $\dot{\kappa}^e_{ij}$ must be

identically zero so that the relation always holds. We hence define

$$\tau^e_{ij} = \frac{\partial \hat{\mathcal{U}}}{\partial \gamma^e_{ij}}, \tag{52}$$

$$\eta = \frac{\partial \hat{\mathcal{U}}}{\partial \rho}, \tag{53}$$

$$p^t = \rho\eta - \mathcal{U}, \tag{54}$$

$$\tau_{ij} = \tau^e_{ij} + p^t\delta_{ij}, \tag{55}$$

$$\mu_{ij} = \frac{\partial \hat{\mathcal{U}}}{\partial \kappa^e_{ij}}, \tag{56}$$

$$E_B = -\frac{\partial \hat{\mathcal{U}}}{\partial B}, \tag{57}$$

where we will call τ^e_{ij} the elastic stress, η is the chemical potential, p^t is a thermodynamic pressure, and E_B is the breakage energy. The couple stresses and breakage energy are standard for Cosserat Breakage Mechanics, but the more refined treatment of the thermodynamics demands consideration of the chemical potential and thermodynamic pressure to correctly obtain the stresses. However, we note that in typical experimental conditions for dry granular media the thermodynamic pressure p^t is negligible. Then, the dissipation is given by what remains after removing the parts acting on the elastic rates:

$$\mathcal{D} = \tau^e_{ij}\dot{\gamma}^p_{ij} + \mu_{ij}\dot{\kappa}^p_{ij} + E_B\dot{B} \geq 0. \tag{58}$$

Now, we need to obtain a time-evolution law for the solid fraction. Re-arranging (16) and applying the time derivative, we get

$$\dot{\rho} = \dot{\phi}\rho_s + \phi\dot{\rho}_s. \tag{59}$$

Then, after using our constitutive assumption (41), we have the total density rate

$$\dot{\rho} = \rho_s\dot{\phi} + \phi\rho_s\chi\dot{\varepsilon}^e_v, \tag{60}$$

which can be equated with the time rate of the density given by rearranging (49) and substituting in (16):

$$\begin{aligned}
\rho_s\dot{\phi} + \phi\rho_s\chi\dot{\varepsilon}^e_v &= \phi\rho_s\dot{\varepsilon}_v, \\
\dot{\phi} &= \phi\dot{\varepsilon}_v - \phi\chi\dot{\varepsilon}^e_v, \\
&= \phi(\dot{\varepsilon}^e_v + \dot{\varepsilon}^p_v) - \phi\chi\dot{\varepsilon}^e_v, \\
&= \phi\left[(1-\chi)\dot{\varepsilon}^e_v + \dot{\varepsilon}^p_v\right],
\end{aligned} \tag{61}$$

which recovers the expression given in Alaei et al. (2021). This also allows us to attribute elastic and plastic components to the rate of the solid fraction:

$$\dot{\phi}^e = \phi(1-\chi)\dot{\varepsilon}^e_v, \tag{62}$$

$$\dot{\phi}^p = \phi\dot{\varepsilon}^p_v. \tag{63}$$

Now, we return to the dissipation expression given in (58) and rearrange it

$$\begin{aligned}
d &= \tau^e_{ij}\dot{\gamma}^p_{ij} + \mu_{ij}\dot{\kappa}^p_{ij} + E_B\dot{B} \geq 0, \\
&= \left(p^e\delta_{ij} + s^e_{ij}\right)\left(\frac{1}{3}\dot{\varepsilon}^p_v\delta_{ij} + \dot{e}^p_{ij}\right) + \left(\frac{1}{3}\mu_{kk}\delta_{ij} + m_{ij}\right)\left(\frac{1}{3}\dot{\kappa}^p_{kk} + \dot{z}^p_{ij}\right) + E_B\dot{B} \geq 0, \\
&= p^e\dot{\varepsilon}^p_v + s^e_{ij}\dot{e}^p_{ij} + m_{ij}\dot{z}^p_{ij} + E_B\dot{B} \geq 0, \\
&= \frac{p^e}{\phi}\dot{\phi}^p + s^e_{ij}\dot{e}^p_{ij} + m_{ij}\dot{z}^p_{ij} + E_B\dot{B} \geq 0, \\
&= \frac{p^e}{\phi}\dot{\phi}^p + q\dot{\gamma}^p_s + E_B\dot{B} \geq 0,
\end{aligned} \tag{64}$$

where to pass from the first line to the second line we expanded the stress and couple-stress terms into their trace and deviatoric parts, to pass from the second line to the third we applied our assumption that the trace parts of the couple-stress do no work (nor store any energy), from the third to the fourth we used (63), and from the fourth to the fifth we used the fact that the weighting factors in our invariants are those for which the equality $q\dot{\gamma}^p_s = s_{ij}\dot{e}^p_{ij} + m_{ij}\dot{z}^p_{ij}$ holds (Collins-Craft, 2019). Now, substituting in the flow rules (30), (31) and (32) we obtain:

$$\begin{aligned}
0 \leq &\frac{p^e}{\phi}\cdot\lambda\left(\sqrt{\frac{E_B}{E_c}}(1-B) - \zeta\chi\right)\frac{2\phi(1-B)}{p^e}\sqrt{\frac{E_B}{E_c}}\sin^2(\omega) + \lambda\frac{2q^2}{(Mp^e + \phi(1-B)c)^2} \\
&+ E_B\lambda\left\langle\sqrt{\frac{E_B}{E_c}}(1-B) - \zeta\chi\right\rangle\frac{2(1-B)}{\sqrt{E_BE_c}}\cos^2(\omega).
\end{aligned} \tag{65}$$

We have that the parameters E_c, ζ, c are all positive, the variables ϕ, B, E_B likewise, the function M_0 is positive for all admissible values which in turn guarantees that M is also positive, $0 \leq \omega \leq \pi/2$ and λ is non-negative. We consider only the case of positive p^e in this model, as tensile failure is governed by different physics (macroscopic cracking) that requires dramatically different models to address. In combination with the Macaulay brackets all these restrictions on the values of the variables guarantee that the third term is non-negative. The second term is composed of a ratio of two squared terms and thus is straightforwardly never negative. In the case of $F \geq 0$, the first term is also straightforwardly non-negative given our restrictions on the variable values. For $F < 0$, the analysis is slightly more complicated. We return to (29) and rearrange it in terms of q^2 and F to obtain $q^2 = (1 - F^2)(Mp^e + \phi(1 - B)c)^2$. Substituting this back in to (65), cancelling out the common factors and suppressing the third term as we have assumed $F < 0$, we have

$$(1 - B)\sqrt{\frac{E_B}{E_c}}\sin^2(\omega)F + 1 - F^2 \geq 0. \tag{66}$$

As we have assumed $F < 0$ we also have $\omega = \pi/2$ and hence $\sin^2(\omega) = 1$, so we can remove it from the equation. We recall also that the value of $\sqrt{E_B/E_c}(1 - B)$ is conditioned by our choice of F, namely $\sqrt{E_B/E_c}(1 - B) = F + \zeta\chi$. Substituting this relationship back in to (66) we have

$$\begin{aligned}(F + \zeta\chi)F + 1 - F^2 &\geq 0,\\ F^2 + \zeta\chi F + 1 - F^2 &\geq 0,\\ 1 + \zeta\chi F &\geq 0.\end{aligned} \tag{67}$$

We see that this inequality is respected for all admissible values ($\zeta \in [0, 1], \chi \in [0, 1], F \in [-1, 0)$) coherent with our assumption of $F < 0$. This guarantees thermodynamic admissibility for $-1 \leq F < 0$, and in combination with the demonstrations above for $F \geq 0$ we have demonstrated that the dissipation relationship (65) is respected for *all* admissible values of the variables.

A.2 Plastic multiplier

In order to (analytically) close the model, the plastic multiplier λ must be calculated. This is achieved by enforcing the consistency condition *i.e.* $y = \dot{y} = 0$ for continued inelastic loading. We exploit automatic differentiation to obtain the quantities $\frac{\partial y}{\partial \gamma^e_{kl}}$, $\frac{\partial y}{\partial \kappa^e_{kl}}$, $\frac{\partial y}{\partial \rho}$, $\frac{\partial y}{\partial \phi}$, $\frac{\partial y}{\partial B}$, which propagates the derivatives through the system using the chain rule. Hence, we obtain in symbolic form

$$\lambda = \frac{\left(\frac{\partial y}{\partial \gamma^e_{kl}} + \frac{\partial y}{\partial \rho}\frac{\partial \rho}{\partial \dot{\gamma}_{kl}} + \frac{\partial y}{\partial \phi}\frac{\partial \dot{\phi}^e}{\partial \dot{\varepsilon}^e_v}\frac{\partial \dot{\varepsilon}^e_v}{\partial \dot{\gamma}^e_{kl}}\right)\dot{\gamma}_{kl} + \frac{\partial y}{\partial \kappa^e_{kl}}\dot{\kappa}_{kl}}{\frac{\partial y}{\partial \gamma^e_{kl}}\overline{\gamma^p_{kl}} + \frac{\partial y}{\partial \kappa^e_{kl}}\overline{\kappa^p_{kl}} + \frac{\partial y}{\partial \phi}\left(\frac{\partial \dot{\phi}^e}{\partial \dot{\varepsilon}^e_v}\frac{\partial \dot{\varepsilon}^e_v}{\partial \dot{\gamma}^e_{kl}}\overline{\gamma^p_{kl}} - \overline{\phi^p}\right) - \frac{\partial y}{\partial B}\overline{B}}, \tag{68}$$

where by $\overline{B}$, $\overline{\phi^p}$, $\overline{\gamma^p_{kl}}$, and $\overline{\kappa^p_{kl}}$ we mean the non-λ parts of the flow rules (30), (31), (36) and (37).

A.3 Incremental constitutive response

While the model is closed by calculating λ, it is convenient to write an expression for the incremental constitutive response, taking into account the appropriate cross-couplings between stresses and couple-stresses with the strain and curvature rates. We make a linear decomposition of λ:

$$\lambda = \lambda^\gamma_{kl}\dot{\gamma}_{kl} + \lambda^\kappa_{kl}\dot{\kappa}_{kl}. \tag{69}$$

By differentiating the stress and couple-stress with respect to time, using (69) and inserting the appropriate flow rules, we may write the incremental constitutive relationship under continued plastic loading as

$$\begin{bmatrix}\dot{\tau}_{ij}\\ \dot{\mu}_{ij}\end{bmatrix} = \begin{bmatrix}E^{ep}_{ijkl} & F^{ep}_{ijkl}\\ K^{ep}_{ijkl} & M^{ep}_{ijkl}\end{bmatrix}\begin{bmatrix}\dot{\gamma}_{kl}\\ \dot{\kappa}_{kl}\end{bmatrix}, \tag{70}$$

where the continuum incremental elastoplastic stiffness matrices are given by

$$E^{ep}_{ijkl} = \frac{\partial \tau_{ij}}{\partial \gamma^e_{kl}} + \frac{\partial \tau_{ij}}{\partial \rho}\frac{\partial \dot{\rho}}{\partial \dot{\gamma}_{kl}} - \left(\frac{\partial \tau_{ij}}{\partial \gamma^e_{kl}}\overline{\gamma^p_{kl}} + \frac{\partial \tau_{ij}}{\partial \kappa^e_{kl}}\overline{\kappa^p_{kl}} - \frac{\partial \tau_{ij}}{\partial B}\overline{B}\right)\lambda^\gamma_{kl}, \tag{71}$$

$$F^{ep}_{ijkl} = \frac{\partial \tau_{ij}}{\partial \kappa^e_{kl}} - \left(\frac{\partial \tau_{ij}}{\partial \gamma^e_{kl}}\overline{\gamma^p_{kl}} + \frac{\partial \tau_{ij}}{\partial \kappa^e_{kl}}\overline{\kappa^p_{kl}} - \frac{\partial \tau_{ij}}{\partial B}\overline{B}\right)\lambda^\kappa_{kl}, \tag{72}$$

$$K^{ep}_{ijkl} = \frac{\partial \mu_{ij}}{\partial \gamma^e_{kl}} + \frac{\partial \mu_{ij}}{\partial \rho}\frac{\partial \dot{\rho}}{\partial \dot{\gamma}_{kl}} - \left(\frac{\partial \mu_{ij}}{\partial \gamma^e_{kl}}\overline{\gamma^p_{kl}} + \frac{\partial \mu_{ij}}{\partial \kappa^e_{kl}}\overline{\kappa^p_{kl}} - \frac{\partial \mu_{ij}}{\partial B}\overline{B}\right)\lambda^\gamma_{kl}, \tag{73}$$

$$M^{ep}_{ijkl} = \frac{\partial \mu_{ij}}{\partial \kappa^e_{kl}} - \left(\frac{\partial \mu_{ij}}{\partial \gamma^e_{kl}}\overline{\gamma^p_{kl}} + \frac{\partial \mu_{ij}}{\partial \kappa^e_{kl}}\overline{\kappa^p_{kl}} - \frac{\partial \mu_{ij}}{\partial B}\overline{B}\right)\lambda^\kappa_{kl}. \tag{74}$$

We emphasise here that the stress that is differentiated with respect to the state variables is the total stress, inclusive of the thermodynamic pressure, and we once again exploit automatic differentiation to obtain the necessary quantities.

A.4 Permeability evolution

As in this work, we are interested in the effect of changes in the microstructure on the global properties of the fault, we use the microstructural information to observe the changes in the permeability of the fault material as it evolves. It is well-established in the literature that the permeability plays a key role in controlling the behaviour of the fault, due to the tight coupling between hydraulic and mechanical effects (Rice, 2006; Rattez, 2017; Rattez et al., 2018a,b,c; Stathas and Stefanou, 2023). In general, we expect that increases in the solid fraction will in turn decrease the permeability of the system (and *vice versa*) in a nonlinear way, as not only will the amount of space available for the fluid to flow through change, but the tortuosity will as well. Similarly, we expect that as the grains break, the permeability should reduce due to the increase in tortuosity of the sample. Following Nguyen and Einav (2009) (who in turn follow Matyka et al. (2008)) in developing a modified Kozeny–Carman equation, we suppose a tortuosity function that depends on the solid fraction $T(\phi) \propto (1-\phi)^{-5}$. Then, for an initial permeability k_0 associated with the initial solid fraction ϕ_0, the ratio of the current permeability k to the original permeability is given by

$$\mathcal{R} = \frac{k}{k_0} = \frac{(1-\phi)^3 {T_0}^2 {d_H}^2}{(1-\phi_0)^3 T^2 {d_{H0}}^2}. \tag{75}$$

B Determining the localisation width in finite element simulations

While the finite element simulations return localisation widths that are visually clear, in order to obtain a quantitative measure, we must conduct a fitting process. In order to maintain coherence with the assumption of the linear stability analysis, we choose to fit a cosine curve to the localisation, fitting on the value of B and the value of γ^p_{21}. We choose these two values as γ^p_{21} is coherent with all plasticity models on which localisation analysis can be conducted, while B gives an indication of the shear band width available only to models belonging to the Breakage Mechanics family. The best-fit cosine is re-found at each time step.

For a given time step, we first set c, a vertical shift parameter to be the value of B or $|\dot{\gamma}_{21}|$ at the upper boundary of the system at that time step, so the function is able to match the values outside of the shear band. Then, we specify the fitting function:

$$\hat{z} = \begin{cases} (A-c)\cos\left(\frac{2\pi x}{\Lambda}\right) + c & \text{if } \left|\frac{2\pi x}{\Lambda}\right| \leq \frac{\pi}{2}, \\ c & \text{if } \left|\frac{2\pi x}{\Lambda}\right| > \frac{\pi}{2}, \end{cases} \tag{76}$$

where $\hat{z}$ is our variable of interest, A is the amplitude parameter and Λ is the wavelength. This function fits a half-wavelength over the localisation, with the height controlled by A and the width controlled by Λ.

At each time step, we then conduct an optimisation using NLopt (Johnson, 2007), in particular the COBYLA algorithm (Powell, 1994, 1998), to find the values of the parameters that minimise the least-squares difference between the values of the variable predicted by the fitting function and the values of the variables that were generated by the finite element simulation. We initialise the parameters with an initial guess of $\{A, \Lambda\} = \{\arg\max_{x\in\mathcal{V}}(\hat{z}, t), 5.0\}$ where t is the time at the current time step. We apply lower bounds of $\{A_{\text{lower}}, \Lambda_{\text{lower}}\} = \{0.75 \times \arg\max_{x\in\mathcal{V}}(\hat{z}, t), 0.0001\}$ and upper bounds of $\{A_{\text{upper}}, \Lambda_{\text{upper}}\} = \{1.5 \times \arg\max_{x\in\mathcal{V}}(\hat{z}, t), 100.0\}$. We only conduct the fitting if the any of the points are on the yield surface, as measured by $\arg\max_{x\in\mathcal{V}}(y, t) \geq -1 \times 10^{-6}$, where y is the value of the yield function. We show a representative comparison of the fitted curves in Figure 21.

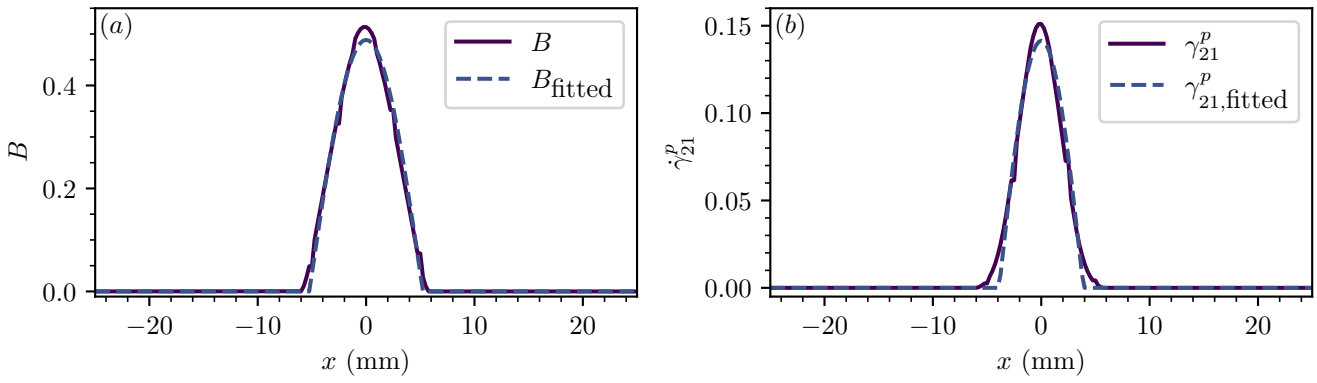

Figure 21: Representative best-fits using a cosine fitting function over the values generated by the simulation of constant volume shearing with $p_0 = 200$ MPa and $\chi_0 = 0.5$, taken at $\Delta\gamma_{21} = 0.02$. (a) The distribution of generated and fitted values of B over the spatial dimension x, and (b) the distribution of generated and fitted values of γ^p_{21} over the spatial dimension x.

We can see that the shape of the localisation generated by the finite element simulation does not perfectly correspond to a cosine curve (nor is it perfectly centred within the simulation) but it is also not dramatically different and the cosine function satisfactorily captures the width of the shear band, which is the key requirement of the method. The quantitative value of the shear band width is obtained by dividing Λ by two at each time step. In order to obtain the initial shear band width, we find the time step at which the fitting parameters are non-zero, and take the values from two time steps after that point, in order to allow the localisation to better reflect the material properties, rather than the initial imperfection.

References

Abdallah, Y. et al. (Jan. 2021). "Compaction Banding in High-Porosity Carbonate Rocks: 1. Experimental Observations". In: *Journal of Geophysical Research: Solid Earth* 126.1. ISSN: 2169-9313. DOI: 10.1029/2020JB020538.

Alaei, E., B. Marks and I. Einav (June 2021). "A Hydrodynamic-Plastic Formulation for Modelling Sand Using a Minimal Set of Parameters". In: *Journal of the Mechanics and Physics of Solids* 151, p. 104388. ISSN: 00225096. DOI: 10.1016/j.jmps.2021.104388.

— (Nov. 2022). "A Five-Parameter Hydrodynamic-Plastic Model for Crushable Sand". In: *International Journal of Solids and Structures* 254–255, p. 111914. ISSN: 0020-7683. DOI: 10.1016/j.ijsolstr.2022.111914.

Alshibli, K.A. and S. Sture (June 2000). "Shear Band Formation in Plane Strain Experiments of Sand". In: *Journal of Geotechnical and Geoenvironmental Engineering* 126.6, pp. 495–503. ISSN: 1090-0241. DOI: 10.1061/(ASCE)1090-0241(2000)126:6(495).

An, L.-J and G. Sammis C (Mar. 1994). "Particle Size Distribution of Cataclastic Fault Materials from Southern California: A 3-D Study". In: *pure and applied geophysics* 143.1-3, pp. 203–227. ISSN: 0033-4553, 1420-9136. DOI: 10.1007/BF00874329.

Andò, E. et al. (2012). "Grain-Scale Experimental Investigation of Localised Deformation in Sand: A Discrete Particle Tracking Approach". In: *Acta Geotechnica* 7.1, pp. 1–13. ISSN: 18611125. DOI: 10.1007/s11440-011-0151-6.

Aydin, A. and A.M. Johnson (1978). "Development of Faults as Zones of Deformation Bands and as Slip Surfaces in Sandstone". In: *Pure and Applied Geophysics PAGEOPH* 116.4-5, pp. 931–942. ISSN: 00334553. DOI: 10.1007/BF00876547.

— (1983). "Analysis of Faulting in Porous Sandstones". In: *Journal of Structural Geology* 5.1, pp. 19–31. ISSN: 01918141. DOI: 10.1016/0191-8141(83)90004-4.

Bandini, V. and M.R. Coop (2011). "The Influence of Particle Breakage on the Location of the Critical State Line of Sands". In: *Soils and Foundations* 51.4, pp. 591–600. ISSN: 00380806. DOI: 10.3208/sandf.51.591.

Bardet, J.-P. and I. Vardoulakis (2001). "Asymmetry of Stress in Granular Media". In: *International Journal of Solids and Structures* 38.2, pp. 353–367. ISSN: 00207683. DOI: 10.1016/S0020-7683(00)00021-4.

Barras, F. and N. Brantut (Jan. 2025). "Shear Localisation Controls the Dynamics of Earthquakes". In: *Nature Communications* 16.1, p. 711. ISSN: 2041-1723. DOI: 10.1038/s41467-024-55363-y.

Baud, P., V. Vajdova and T.-F. Wong (2006). "Shear-Enhanced Compaction and Strain Localization: Inelastic Deformation and Constitutive Modeling of Four Porous Sandstones". In: *Journal of Geophysical Research: Solid Earth* 111.12, pp. 1–17. ISSN: 21699356. DOI: 10.1029/2005JB004101.

Benammar, C. et al. (2025). "Grain Breakage in Shear Bands and Its Effect on the Permeability Decrease of Granular Material Specimens during Triaxial Loading". In: *Acta Geodynamica et Geomaterialia*, pp. 317–332. ISSN: 1214-

9705. DOI: 10.13168/AGG.2025.0022. URL: http://www.irsm.cas.cz/index_en.php?page=acta_detail_doi&id=540.

Bésuelle, P., J. Desrues and S. Raynaud (2000). "Experimental Characterisation of the Localisation Phenomenon inside a Vosges Sandstone in a Triaxial Cell". In: *International Journal of Rock Mechanics and Mining Sciences* 37.8, pp. 1223–1237. ISSN: 13651609. DOI: 10.1016/S1365-1609(00)00057-5.

Bolton, M.D. (Mar. 1986). "The Strength and Dilatancy of Sands". In: *Géotechnique* 36.1, pp. 65–78. ISSN: 0016-8505, 1751-7656. DOI: 10.1680/geot.1986.36.1.65.

Brantut, N., I. Stefanou and J. Sulem (2017). "Dehydration-Induced Instabilities at Intermediate Depths in Subduction Zones". In: *Journal of Geophysical Research: Solid Earth* 122.8, pp. 6087–6107. ISSN: 21699356. DOI: 10.1002/2017JB014357.

Brantut, N. and J. Sulem (2012). "Strain Localization and Slip Instability in a Strain-Rate Hardening, Chemically Weakening Material". In: *Journal of Applied Mechanics, Transactions ASME* 79.3, pp. 1–10. ISSN: 00218936. DOI: 10.1115/1.4005880.

Brantut, N., J. Sulem and A. Schubnel (May 2011). "Effect of Dehydration Reactions on Earthquake Nucleation: Stable Sliding, Slow Transients, and Unstable Slip". In: *Journal of Geophysical Research* 116.B5, B05304. ISSN: 0148-0227. DOI: 10.1029/2010JB007876.

Buscarnera, G. and A. Das (June 2016). "Chemo-Mechanics of Cemented Granular Solids Subjected to Precipitation and Dissolution of Mineral Species". In: *International Journal for Numerical and Analytical Methods in Geomechanics* 40.9, pp. 1295–1320. ISSN: 03639061. DOI: 10.1002/nag.2486.

Buscarnera, G. and I. Einav (2012). "The Yielding of Brittle Unsaturated Granular Soils". In: *Geotechnique* 62.2, pp. 147–160. ISSN: 00168505. DOI: 10.1680/geot.10.P.118.

Carbillet, L. et al. (2022). "The Influence of Grain Size Distribution on Mechanical Compaction and Compaction Localization in Porous Rocks". In: *Journal of Geophysical Research: Solid Earth* 127.11, e2022JB025216. ISSN: 2169-9356. DOI: 10.1029/2022JB025216. URL: https://onlinelibrary.wiley.com/doi/abs/10.1029/2022JB025216.

Cashman, S. and K. Cashman (2000). "Cataclasis and Deformation-Band Formation in Unconsolidated Marine Terrace Sand, Humboldt County, California". In: *Geology* 28.2, pp. 111–114. ISSN: 00917613. DOI: 10.1130/0091-7613(2000)28<111:CADFIU>2.0.CO;2.

Chambon, G., J. Schmittbuhl and A. Corfdir (2002). "Laboratory Gouge Friction: Seismic-like Slip Weakening and Secondary Rate- and State-Effects". In: *Geophysical Research Letters* 29.10, pp. 4-1-4–4. ISSN: 0094-8276. DOI: 10.1029/2001gl014467.

Charalampidou, E.M. et al. (2011). "Characterization of Shear and Compaction Bands in a Porous Sandstone Deformed under Triaxial Compression". In: *Tectonophysics* 503, pp. 8–17. ISSN: 00401951. DOI: 10.1016/j.tecto.2010.09.032.

Chen, Y. and I. Einav (Apr. 2024). "A Hydrodynamic Finite Element Model for Chemo-Mechanically Loaded Poroelastic Materials". In: *Computers and Geotechnics* 168, p. 106161. ISSN: 0266-352X. DOI: 10.1016/j.compgeo.2024.106161.

Chen, Y., F. Guillard and I. Einav (2023). "A Hydrodynamic Model for Chemo-Mechanics of Poroelastic Materials". In: *Géotechnique* 74.13, pp. 1713–1728. ISSN: 0016-8505. DOI: 10.1680/jgeot.22.00260.

Chester, F.M. and J.S. Chester (1998). "Ultracataclasite Structure and Friction Processes of the Punchbowl Fault, San Andreas System, California". In: *Tectonophysics* 295.1-2, pp. 199–221. ISSN: 00401951. DOI: 10.1016/S0040-1951(98)00121-8.

Cil, M.B., R.C. Hurley and L. Graham-Brady (2020). "Constitutive Model for Brittle Granular Materials Considering Competition between Breakage and Dilation". In: *Journal of Engineering Mechanics* 146.1, pp. 1–12. ISSN: 07339399. DOI: 10.1061/(ASCE)EM.1943-7889.0001690.

Collins-Craft, N.A. (2019). "The Effect of Evolving Micro-Structural Length Scale on the Macroscopic Constitutive Behaviour of Granular Media". PhD thesis. The University of Sydney & Université Paris-Est.

Collins-Craft, N.A. et al. (Aug. 2020). "A Cosserat Breakage Mechanics Model for Brittle Granular Media". In: *Journal of the Mechanics and Physics of Solids* 141, p. 103975. ISSN: 00225096. DOI: 10.1016/j.jmps.2020.103975.

Cosserat, E. and F. Cosserat (1909). *Théorie Des Corps Déformables*. Paris: Librairie Scientifique A. Hermann et Fils.

Couture, C. and P. Bésuelle (May 2022). "A True Triaxial Experimental Study on Porous Vosges Sandstone: From Strain Localization Precursors to Failure Using Full-Field Measurements". In: *International Journal of Rock Mechanics and Mining Sciences* 153, p. 105031. ISSN: 13651609. DOI: 10.1016/j.ijrmms.2021.105031.

— (July 2023). "Three-Invariant Model and Bifurcation Analysis of Deformation Bands for a Sandstone Subjected to True Triaxial Loading Paths". In: *Acta Geotechnica* 18.7, pp. 3421–3434. ISSN: 1861-1133. DOI: 10.1007/s11440-023-01811-w.

Das, A., G.D. Nguyen and I. Einav (2011). "Compaction Bands Due to Grain Crushing in Porous Rocks: A Theoretical Approach Based on Breakage Mechanics". In: *Journal of Geophysical Research: Solid Earth* 116.8, pp. 1–14. ISSN: 21699356. DOI: 10.1029/2011JB008265.

— (2013). "The Propagation of Compaction Bands in Porous Rocks Based on Breakage Mechanics". In: *Journal of Geophysical Research: Solid Earth* 118.5, pp. 2049–2066. ISSN: 21699356. DOI: 10.1002/jgrb.50193.

Das, A. et al. (2014). "A Thermomechanical Constitutive Model for Cemented Granular Materials with Quantifiable Internal Variables. Part II - Validation and Localization Analysis". In: *Journal of the Mechanics and Physics of Solids* 70.1, pp. 382–405. ISSN: 00225096. DOI: 10.1016/j.jmps.2014.05.022. URL: http://dx.doi.org/10.1016/j.jmps.2014.05.022.

Dautriat, J. et al. (1st July 2009). "Axial and Radial Permeability Evolutions of Compressed Sandstones: End Effects and Shear-band Induced Permeability Anisotropy". In: *Pure and Applied Geophysics* 166.5, pp. 1037–1061. ISSN: 1420-9136. DOI: 10.1007/s00024-009-0495-0. URL: https://doi.org/10.1007/s00024-009-0495-0.

de Borst, R. and T. Duretz (2020). "On Viscoplastic Regularisation of Strain-Softening Rocks and Soils". In: *International Journal for Numerical and Analytical Methods in Geomechanics* 44.6, pp. 890–903. ISSN: 10969853. DOI: 10.1002/nag.3046.

Desrues, J. and G. Viggiani (2004). "Strain Localization in Sand: An Overview of the Experimental Results Obtained in Grenoble Using Stereophotogrammetry". In: *International Journal for Numerical and Analytical Methods in Geomechanics* 28.4, pp. 279–321. ISSN: 03639061. DOI: 10.1002/nag.338.

Desrues, J. et al. (2018). "How Does Strain Localise in Standard Triaxial Tests on Sand: Revisiting the Mechanism 20 Years On". In: *Mechanics Research Communications* 92, pp. 142–146. ISSN: 00936413. DOI: 10.1016/j.mechrescom.2018.08.007.

Doré-Ossipyan, C. et al. (2025). "Synchrotron 4D X-Ray Computed Tomography of a Porous Limestone: Influence of Porosity on Deformation Mechanisms at Multiple Scales". In: *Journal of Geophysical Research: Solid Earth* 130.10, e2025JB031620. ISSN: 2169-9356. DOI: 10.1029/2025JB031620. URL: https://onlinelibrary.wiley.com/doi/abs/10.1029/2025JB031620.

Einav, I. (2007a). "Breakage Mechanics-Part I: Theory". In: *Journal of the Mechanics and Physics of Solids* 55.6, pp. 1274–1297. ISSN: 00225096. DOI: 10.1016/j.jmps.2006.11.003.

— (2007b). "Breakage Mechanics-Part II: Modelling Granular Materials". In: *Journal of the Mechanics and Physics of Solids* 55.6, pp. 1298–1320. ISSN: 00225096. DOI: 10.1016/j.jmps.2006.11.004.

— (2007c). "Fracture Propagation in Brittle Granular Matter". In: *Proceedings of the Royal Society A: Mathematical, Physical and Engineering Sciences* 463.2087, pp. 3021–3035. ISSN: 14712946. DOI: 10.1098/rspa.2007.1898.

— (2007d). "Soil Mechanics: Breaking Ground". In: *Philosophical Transactions of the Royal Society A: Mathematical, Physical and Engineering Sciences* 365.1861, pp. 2985–3002. ISSN: 1364503X. DOI: 10.1098/rsta.2007.0009.

— (2012). "The Unification of Hypo-Plastic and Elasto-Plastic Theories". In: *International Journal of Solids and Structures* 49.11-12, pp. 1305–1315. ISSN: 00207683. DOI: 10.1016/j.ijsolstr.2012.02.003.

El Bied, A., J. Sulem and F. Martineau (2002). "Microstructure of Shear Zones in Fontainebleau Sandstone". In: *International Journal of Rock Mechanics and Mining Sciences* 39.7, pp. 917–932. ISSN: 13651609. DOI: 10.1016/S1365-1609(02)00068-0.

Exner, U. and C. Tschegg (2012). "Preferential Cataclastic Grain Size Reduction of Feldspar in Deformation Bands in Poorly Consolidated Arkosic Sands". In: *Journal of Structural Geology* 43, pp. 63–72. ISSN: 01918141. DOI: 10.1016/j.jsg.2012.08.005.

Fazio, M., M.R. Chandler and M. Sauter (Sept. 2023). "Permeability Evolution of Bentheim Sandstone at Simulated Georeservoir Conditions". In: *Scientific Reports* 13.1, p. 16171. ISSN: 2045-2322. DOI: 10.1038/s41598-023-42826-3.

Feia, S. et al. (2016). "Changes in Permeability of Sand during Triaxial Loading: Effect of Fine Particles Production". In: *Acta Geotechnica* 11.1, pp. 1–19. ISSN: 18611133. DOI: 10.1007/s11440-014-0351-y.

Fossen, H. et al. (July 2007). "Deformation Bands in Sandstone: A Review". In: *Journal of the Geological Society* 164.4, pp. 755–769. ISSN: 0016-7649. DOI: 10.1144/0016-76492006-036.

Froiio, F. and A. Zervos (24th Mar. 2019). "Second-Grade Elasticity Revisited". In: *Mathematics and Mechanics of Solids* 24.3, pp. 748–777. ISSN: 1081-2865. DOI: 10.1177/1081286518754616. URL: http://journals.sagepub.com/doi/10.1177/1081286518754616.

Froiio, F., A. Zervos and I. Vardoulakis (2010). "On Natural Boundary Conditions in Linear 2nd-Grade Elasticity". In: *Mechanics of Generalized Continua: One Hundred Years After the Cosserats*. Ed. by G.A. Maugin and A.V. Metrikine. New York, NY: Springer, pp. 211–221. ISBN: 978-1-4419-5695-8. DOI: 10.1007/978-1-4419-5695-8_22. URL: https://doi.org/10.1007/978-1-4419-5695-8_22.

Germain, P. (Nov. 1973). "The Method of Virtual Power in Continuum Mechanics. Part 2: Microstructure". In: *SIAM Journal on Applied Mathematics* 25.3, pp. 556–575. ISSN: 0036-1399. DOI: 10.1137/0125053.

Gerolymatou, E., A. Stathas and I. Stefanou (July 2024). "Do Multiphysics Processes Lead to Mesh Independent Analyses?" In: *International Journal of Mechanical Sciences* 274, p. 109265. ISSN: 00207403. DOI: 10.1016/j.ijmecsci.2024.109265.

Haines, T.J. et al. (Apr. 2016). "Permeability Evolution across Carbonate Hosted Normal Fault Zones". In: *Marine and Petroleum Geology* 72, pp. 62–82. ISSN: 0264-8172. DOI: 10.1016/j.marpetgeo.2016.01.008.

Hall, S.A. et al. (May 2010). "Discrete and Continuum Analysis of Localised Deformation in Sand Using X-ray μCT and Volumetric Digital Image Correlation". In: *Géotechnique* 60.5, pp. 315–322. ISSN: 0016-8505. DOI: 10.1680/geot.2010.60.5.315. URL: http://www.icevirtuallibrary.com/doi/10.1680/geot.2010.60.5.315.

Hardin, B.O. and V.P. Drnevich (June 1972). "Shear Modulus and Damping in Soils: Measurement and Parameter Effects (Terzaghi Leture)". In: *Journal of the Soil Mechanics and Foundations Division* 98.6, pp. 603–624. ISSN: 0044-7994, 2690-3369. DOI: 10.1061/jsfeaq.0001756.

Heap, M.J. et al. (2015). "Time-Dependent Compaction Band Formation in Sandstone". In: *Journal Geophysical Research: Solid Earth* 120, pp. 4808–4830. DOI: 10.1002/2015JB012022.Received.

Heimisson, E.R. et al. (2022). "A Spectral Boundary-Integral Method for Faults and Fractures in a Poroelastic Solid: Simulations of a Rate-and-State Fault With Dilatancy, Compaction, and Fluid Injection". In: *Journal of Geophysical Research: Solid Earth* 127.9, e2022JB024185. ISSN: 2169-9356. DOI: 10.1029/2022JB024185.

Jacquey, A.B., H. Rattez and E. Veveakis (July 2021). "Strain Localization Regularization and Patterns Formation in Rate-Dependent Plastic Materials with Multiphysics Coupling". In: *Journal of the Mechanics and Physics of Solids* 152, p. 104422. ISSN: 00225096. DOI: 10.1016/j.jmps.2021.104422.

Jiang, Y. and M. Liu (2009). "Granular Solid Hydrodynamics". In: *Granular Matter* 11.3, pp. 139–156. ISSN: 14345021. DOI: 10.1007/s10035-009-0137-3.

[SW] Johnson, S.G., *The NLopt nonlinear-optimization package* 2007. SWHID: ⟨swh:1:dir:0a9fa204d8ed9e2f88795013ddd59cfb1a2029e7;origin=https://github.com/stevengj/nlopt;visit=swh:1:snp:46dc48703f89a2764bb304190924820cdf6ced8e;anchor=swh:1:rev:7a7587e5ef1cb15f412515d852d1fc261c863e96⟩.

Karatza, Z. et al. (2018). "Evolution of Deformation and Breakage in Sand Studied Using X-ray Tomography". In: *Geotechnique* 68.2, pp. 107–117. ISSN: 17517656. DOI: 10.1680/jgeot.16.P.208.

Kendall, K (1978). "The Impossibility of Comminuting Small Particles by Compression". In: *Nature* 272.April, pp. 710–711.

Klein, E. and T. Reuschlé (May 2003). "A Model for the Mechanical Behaviour of Bentheim Sandstone in the Brittle Regime". In: *Pure and Applied Geophysics* 160.5, pp. 833–849. ISSN: 1420-9136. DOI: 10.1007/PL00012568.

Klein, E. et al. (2001). "Mechanical Behaviour and Failure Mode of Bentheim Sandstone under Triaxial Compression". In: *Physics and Chemistry of the Earth, Part A: Solid Earth and Geodesy* 26.1-2, pp. 21–25. ISSN: 14641895. DOI: 10.1016/S1464-1895(01)00017-5.

Lade, P.V. and P.A. Bopp (Feb. 2005). "Relative Density Effects on Drained Sand Behavior at High Pressures". In: *Soils and Foundations* 45.1, pp. 1–13. DOI: 10.3208/sandf.45.1_1.

Lommatzsch, M. et al. (2015). "Dilatant Shear Band Formation and Diagenesis in Calcareous, Arkosic Sandstones, Vienna Basin (Austria)". In: *Marine and Petroleum Geology* 62, pp. 144–160. ISSN: 02648172. DOI: 10.1016/j.marpetgeo.2015.02.002.

Manzocchi, T., P.S. Ringrose and J.R. Underhill (Jan. 1998). "Flow through Fault Systems in High-Porosity Sandstones". In: *Geological Society, London, Special Publications* 127.1, pp. 65–82. ISSN: 0305-8719, 2041-4927. DOI: 10.1144/gsl.sp.1998.127.01.06.

Matyka, M., A. Khalili and Z. Koza (Aug. 2008). "Tortuosity-Porosity Relation in Porous Media Flow". In: *Physical Review E* 78.2, p. 026306. ISSN: 1539-3755, 1550-2376. DOI: 10.1103/PhysRevE.78.026306.

Micarelli, L., A. Benedicto and C.A.J. Wibberley (July 2006). "Structural Evolution and Permeability of Normal Fault Zones in Highly Porous Carbonate Rocks". In: *Journal of Structural Geology* 28.7, pp. 1214–1227. ISSN: 01918141. DOI: 10.1016/j.jsg.2006.03.036. URL: https://linkinghub.elsevier.com/retrieve/pii/S0191814106000873.

Mühlhaus, H.-B. (1986). "Seherfugenanalyse Bei Granularem Material Im Rahmen Der Cosserat-Theorie". In: *Ingenieur-Archiv* 56, pp. 389–399.

Mühlhaus, H.-B. and I. Vardoulakis (1987). "The Thickness of Shear Bands in Granular Materials". In: *Géotechnqiue* 37.3, pp. 271–283.

Neuzil, C.E. (May 2019). "Permeability of Clays and Shales". In: *Annual Review of Earth and Planetary Sciences* 47.Volume 47, 2019, pp. 247–273. ISSN: 0084-6597, 1545-4495. DOI: 10.1146/annurev-earth-053018-060437.

Nguyen, G.D. and I. Einav (2009). "The Energetics of Cataclasis Based on Breakage Mechanics". In: *Pure and Applied Geophysics* 166, pp. 1693–1724. DOI: 10.1007/978-3-0346-0138-2.

— (2010). "Nonlocal Regularisation of a Model Based on Breakage Mechanics for Granular Materials". In: *International Journal of Solids and Structures* 47.10, pp. 1350–1360. ISSN: 00207683. DOI: 10.1016/j.ijsolstr.2010.01.020.

Noël, C., P. Baud and M. Violay (Nov. 2021). "Effect of Water on Sandstone's Fracture Toughness and Frictional Parameters: Brittle Strength Constraints". In: *International Journal of Rock Mechanics and Mining Sciences* 147, p. 104916. ISSN: 13651609. DOI: 10.1016/j.ijrmms.2021.104916.

Ord, A., I. Vardoulakis and R. Kajewski (1991). "Shear Band Formation in Gosford Sandstone". In: *International Journal of Rock Mechanics and Mining Sciences* 28.5, pp. 397–409. ISSN: 01489062. DOI: 10.1016/0148-9062(91)90078-Z.

Papachristos, E., I. Stefanou and J. Sulem (2023). "A Discrete Elements Study of the Frictional Behavior of Fault Gouges". In: *Journal of Geophysical Research: Solid Earth* 128.1, e2022JB025209. ISSN: 2169-9356. DOI: 10.1029/2022JB025209. URL: https://onlinelibrary.wiley.com/doi/abs/10.1029/2022JB025209.

Papamichos, E. (Sept. 2010). "Continua with Microstructure: Cosserat Theory". In: *European Journal of Environmental and Civil Engineering* 14.8-9, pp. 1011–1029. ISSN: 1964-8189, 2116-7214. DOI: 10.1080/19648189.2010.9693277.

Papanastasiou, P.C. and I. Vardoulakis (1989). "Bifurcation Analysis of Deep Boreholes: II. Scale Effect". In: *International Journal for Numerical and Analytical Methods in Geomechanics* 13.5, pp. 183–198. ISSN: 01489062. DOI: 10.1016/0148-9062(89)90982-0.

— (1992). "Numerical Treatment of Progressive Localization in Relation to Borehole Stability". In: *International Journal for Numerical and Analytical Methods in Geomechanics* 16.6, pp. 389–424. ISSN: 10969853. DOI: 10.1002/nag.1610160602.

Papanicolopulos, S.A. and E. Veveakis (2011). "Sliding and Rolling Dissipation in Cosserat Plasticity". In: *Granular Matter* 13.3, pp. 197–204. ISSN: 14345021. DOI: 10.1007/s10035-011-0253-8.

Pijaudier-Cabot, G. and Z.P. Bažant (1988). "Nonlocal Damage Theory". In: *Journal of Engineering Mechanics* 113.10, pp. 1512–1533.

Pinzon, G. et al. (Mar. 2025). "X-Ray Tomography Analysis of Particle Morphology Influence on Granular Deformation Processes". In: *Open Geomechanics* 6, pp. 1–14. ISSN: 2644-9676. DOI: 10.5802/ogeo.21.

Pizzati, M., F. Balsamo and F. Storti (Aug. 2020). "Displacement-Dependent Microstructural and Petrophysical Properties of Deformation Bands and Gouges in Poorly Lithified Sandstone Deformed at Shallow Burial Depth (Crotone Basin, Italy)". In: *Journal of Structural Geology* 137.June 2019, p. 104069. ISSN: 01918141. DOI: 10.1016/j.jsg.2020.104069.

Platt, J.D., N. Brantut and J.R. Rice (2015). "Strain Localization Driven by Thermal Decomposition during Seismic Shear". In: *Journal of Geophysical Research: Solid Earth* 120.6, pp. 4405–4433. ISSN: 21699356. DOI: 10.1002/2014JB011493.

Platt, J.D., J.W. Rudnicki and J.R. Rice (2014). "Stability and Localization of Rapid Shear in Fluid-Saturated Fault Gouge: 2. Localized Zone Width and Strength Evolution". In: *Journal of Geophysical Research: Solid Earth* 119.5, pp. 4334–4359. ISSN: 21699356. DOI: 10.1002/2013JB010711.

PlotDigitizer (2025). URL: https://plotdigitizer.com.

Poh, L.H. and G. Sun (2017). "Localizing Gradient Damage Model with Decreasing Interactions". In: *International Journal for Numerical Methods in Engineering* 110.6, pp. 503–522. ISSN: 10970207. DOI: 10.1002/nme.5364.

Powell, M.J.D. (1994). "A Direct Search Optimization Method That Models the Objective and Constraint Functions by Linear Interpolation". In: *Advances in Optimization and Numerical Analysis*. Ed. by S. Gomez and J.-P. Hennart. Dordrecht: Springer Netherlands, pp. 51–67. ISBN: 978-90-481-4358-0 978-94-015-8330-5. DOI: 10.1007/978-94-015-8330-5_4. URL: http://link.springer.com/10.1007/978-94-015-8330-5_4.

— (1998). "Direct Search Algorithms for Optimization Calculations". In: *Acta Numerica* 7, pp. 287–336. ISSN: 1474-0508, 0962-4929. DOI: 10.1017/S0962492900002841. URL: https://www.cambridge.org/core/journals/acta-numerica/article/direct-search-algorithms-for-optimization-calculations/23FA5B19EAF122E02D3724DB1841238C.

Rattez, H. (2017). "Couplages Thermo-Hydro-Mécaniques et Localisation Dans Les Milieux de Cosserat : Application à l'analyse de Stabilité Du Cisaillement Rapide Des Failles". PhD thesis. Université Paris-Est.

Rattez, H., I. Stefanou and J. Sulem (2018a). "The Importance of Thermo-Hydro-Mechanical Couplings and Microstructure to Strain Localization in 3D Continua with Application to Seismic Faults. Part I: Theory and Linear Stability Analysis". In: *Journal of the Mechanics and Physics of Solids* 115, pp. 54–76. ISSN: 00225096. DOI: 10.1016/j.jmps.2018.03.004.

Rattez, H. et al. (2018b). "Numerical Analysis of Strain Localization in Rocks with Thermo-hydro-mechanical Couplings Using Cosserat Continuum". In: *Rock Mechanics and Rock Engineering* 51.10, pp. 3295–3311. ISSN: 07232632. DOI: 10.1007/s00603-018-1529-7.

— (2018c). "The Importance of Thermo-Hydro-Mechanical Couplings and Microstructure to Strain Localization in 3D Continua with Application to Seismic Faults. Part II: Numerical Implementation and Post-Bifurcation Analysis". In: *Journal of the Mechanics and Physics of Solids* 115, pp. 1–29. ISSN: 00225096. DOI: 10.1016/j.jmps.2018.03.003.

Rattez, H. et al. (Apr. 2022). "Effect of Grain Size Distribution on the Shear Band Thickness Evolution in Sand". In: *Géotechnique* 72.4, pp. 350–363. ISSN: 0016-8505, 1751-7656. DOI: 10.1680/jgeot.20.P.120.

Ray, R. and G. Buscarnera (June 2021). "Simulation of High-Strain-Rate Comminution through a Breakage Model with Adaptive Rate Dependence". In: *Journal of Engineering Mechanics* 147.6, p. 04021030. ISSN: 0733-9399. DOI: 10.1061/(ASCE)EM.1943-7889.0001924.

— (June 2025). "Modeling Rate-Dependent Shearing in Crushable Sand with a Pseudoviscous Kinetic Energy Potential". In: *Journal of Engineering Mechanics* 151.8. DOI: 10.1061/JENMDT.EMENG-8303.

Rice, J.R. (2006). "Heating and Weakening of Faults during Earthquake Slip". In: *Journal of Geophysical Research: Solid Earth* 111.5, pp. 1–29. ISSN: 21699356. DOI: 10.1029/2005JB004006.

Rice, J.R. and J.W. Rudnicki (1980). "A Note on Some Features of the Theory of Localization of Deformation". In: *International Journal of Solids and Structures* 16.7, pp. 597–605. ISSN: 00207683. DOI: 10.1016/0020-7683(80)90019-0.

Rice, J.R., J.W. Rudnicki and J.D. Platt (2014). "Stability and Localization of Rapid Shear in Fluid-Saturated Fault Gouge: 1. Linearized Stability Analysis". In: *Journal of Geophysical Research: Solid Earth* 119.5, pp. 4311–4333. ISSN: 21699356. DOI: 10.1002/2013JB010710.

Riley, D. M., I. Einav and F. Guillard (Feb. 2025). "A Consistent Derivation of Soil Stiffness from Elastic Wave Speeds". In: *Géotechnique*, pp. 1–10. ISSN: 0016-8505, 1751-7656. DOI: 10.1680/jgeot.23.00457.

Rossi, C., A. Tengattini and G. Viggiani (2024). "A Constitutive Model for Lightly Cemented Granular Materials". In: *Computers and Geotechnics* 174, p. 106550. ISSN: 0266352X. DOI: 10.1016/j.compgeo.2024.106550. URL: https://linkinghub.elsevier.com/retrieve/pii/S0266352X24004865.

Rotevatn, A. et al. (2008). "Slipped Deformation Bands: A New Type of Cataclastic Deformation Bands in Western Sinai, Suez Rift, Egypt". In: *Journal of Structural Geology* 30.11, pp. 1317–1331. ISSN: 01918141. DOI: 10.1016/j.jsg.2008.06.010.

Rubin, M.B. and I. Einav (2011). "A Large Deformation Breakage Model of Granular Materials Including Porosity and Inelastic Distortional Deformation Rate". In: *International Journal of Engineering Science* 49.10, pp. 1151–1169. ISSN: 00207225. DOI: 10.1016/j.ijengsci.2011.05.002.

Rudnicki, J.W. and J.R. Rice (1975). "Conditions for the Localization of Deformation in Pressure-Sensitive Dilatant Materials". In: *Journal of the Mechanics and Physics of Solids* 23.6, pp. 371–394. ISSN: 00225096. DOI: 10.1016/0022-5096(75)90001-0.

Sammis, C.G. and R.L. Biegel (1989). "Fractals, Fault-Gouge, and Friction". In: *Pure and Applied Geophysics* 131.1/2, pp. 255–271. DOI: 10.1007/BF00874490.

Sammis, C.G., G. King and R.L. Biegel (1987). "The Kinematics of Gouge Deformation". In: *Pure and Applied Geophysics PAGEOPH* 125.5, pp. 777–812. ISSN: 00334553. DOI: 10.1007/BF00878033.

Sammis, C.G. et al. (1986). "Self-Similar Cataclasis in the Formation of Fault Gouge". In: *Pure and Applied Geophysics* 124.1/2, pp. 53–78. DOI: 10.1007/BF00875719.

Sheng, D., D.M. Pedroso and A.J. Abbo (Oct. 2008). "Non-Convexity and Stress-Path Dependency of Unsaturated Soil Models". In: *Computational Mechanics* 42.5, pp. 685–694. ISSN: 1432-0924. DOI: 10.1007/s00466-008-0268-0.

Sibson, R.H. (2003). "Thickness of the Seismic Slip Zone". In: *Bulletin of the Seismological Society of America* 93.3, pp. 1169–1178. ISSN: 00371106. DOI: 10.1785/0120020061.

Stathas, A. and I. Stefanou (Jan. 2022). "The Role of Viscous Regularization in Dynamical Problems, Strain Localization and Mesh Dependency". In: *Computer Methods in Applied Mechanics and Engineering* 388, p. 114185. ISSN: 00457825. DOI: 10.1016/j.cma.2021.114185.

— (June 2023). "Fault Friction under Thermal Pressurization during Large Seismic-Slip: Numerical Analyses and Extension of the Model of Frictional Slip". In: *International Journal of Mechanical Sciences* 248, p. 108184. ISSN: 0020-7403. DOI: 10.1016/j.ijmecsci.2023.108184.

Stefanou, I. and S. Alevizos (2016). "Fundamentals of Bifurcation Theory and Stability Analysis". In: *Modelling of Instabilities and Bifurcation in Geomechanics*. Ed. by J. Sulem et al. Grenoble: ALERT Geomaterials.

[SW Rel.] Stefanou, I. and A. Stathas, *Numerical Geolab* version 1.0.1, 12th Dec. 2023. IMSIA (UMR 9219), CNRS, EDF, CEA, ENSTA Paris, Institut Polytechnique de Paris, Palaiseau, France and Institut für Konstruktiver Ingenieurbau, Universität für Bodenkultur Wien, Vienna, Austria. LIC: GPL-3.0-only. VCS: https://github.com/AlexSTA1993/numerical_geolab, SWHID: ⟨swh:1:dir:0cdf8bb9499f9a10d4458df650f4c2f2bb3640be;origin=https://github.com/AlexSTA1993/numerical_geolab;visit=swh:1:snp:98f1a88c8a6128a66fd89cbb8b68ec02840e8dc1;anchor=swh:1:rev:ecad099c55f25d5e976c1be5d4a7331e61c859f0⟩.

Stefanou, I. and J. Sulem (2014). "Chemically Induced Compaction Bands: Triggering Conditions and Band Thickness". In: *Journal of Geophysical Research: Solid Earth* 119, pp. 1195–1209. DOI: 10.1002/2013JB010342..

Sulem, J. (2007). "Stress Orientation Evaluated from Strain Localisation Analysis in Aigion Fault". In: *Tectonophysics* 442.1-4, pp. 3–13. ISSN: 00401951. DOI: 10.1016/j.tecto.2007.03.005.

Sulem, J. and H. Ouffroukh (Feb. 2006). "Shear Banding in Drained and Undrained Triaxial Tests on a Saturated Sandstone: Porosity and Permeability Evolution". In: *International Journal of Rock Mechanics and Mining Sciences* 43.2, pp. 292–310. ISSN: 13651609. DOI: 10.1016/j.ijrmms.2005.07.001.

Sulem, J. and I. Stefanou (2016). "Thermal and Chemical Effects in Shear and Compaction Bands". In: *Geomechanics for Energy and the Environment* 6, pp. 4–21. ISSN: 23523808. DOI: 10.1016/j.gete.2015.12.004.

Sulem, J., I. Stefanou and E. Veveakis (June 2011). "Stability Analysis of Undrained Adiabatic Shearing of a Rock Layer with Cosserat Microstructure". In: *Granular Matter* 13.3, pp. 261–268. ISSN: 1434-5021. DOI: 10.1007/s10035-010-0244-1.

Tengattini, A., A. Das and I. Einav (2016). "A Constitutive Modelling Framework Predicting Critical State in Sand Undergoing Crushing and Dilation". In: *Geotechnique* 66.9, pp. 695–710. ISSN: 17517656. DOI: 10.1680/jgeot.14.P.164.

Tengattini, A. et al. (2014). "A Thermomechanical Constitutive Model for Cemented Granular Materials with Quantifiable Internal Variables. Part I - Theory". In: *Journal of the Mechanics and Physics of Solids* 70.1, pp. 281–296. ISSN: 00225096. DOI: 10.1016/j.jmps.2014.05.021. URL: http://dx.doi.org/10.1016/j.jmps.2014.05.021.

Tengattini, A. et al. (2022a). "Micromechanically Inspired Investigation of Cemented Granular Materials: Part I—from X-ray Micro Tomography to Measurable Model Variables". In: *Acta Geotechnica*. ISSN: 1861-1125. DOI: 10.1007/s11440-022-01486-9. URL: https://doi.org/10.1007/s11440-022-01486-9.

Tengattini, A. et al. (2022b). "Micromechanically Inspired Investigation of Cemented Granular Materials: Part II—from Experiments to Modelling and Back". In: *Acta Geotechnica*. ISSN: 1861-1125. DOI: 10.1007/s11440-022-01476-x. URL: https://doi.org/10.1007/s11440-022-01476-x.

Torabi, A. (2014). "Cataclastic Bands in Immature and Poorly Lithified Sandstone, Examples from Corsica, France". In: *Tectonophysics* 630.C, pp. 91–102. ISSN: 00401951. DOI: 10.1016/j.tecto.2014.05.014.

Vajdova, V., P. Baud and T.-F. Wong (2004). "Permeability Evolution during Localized Deformation in Bentheim Sandstone". In: *Journal of Geophysical Research: Solid Earth* 109.B10. ISSN: 2156-2202. DOI: 10.1029/2003JB002942.

Vardoulakis, I. and P.C. Papanastasiou (1988). "Bifurcation Analysis of Deep Boreholes: I. Surface Instabilities". In: *International Journal for Numerical and Analytical Methods in Geomechanics* 12.4, pp. 379–399. ISSN: 10969853. DOI: 10.1002/nag.1610120404.

Vardoulakis, I. and J. Sulem (1995). *Bifurcation Analysis in Geomechanics*. Glasgow: Blackie Academic & Professional. ISBN: 0-7514-0214-1. DOI: 10.1201/9781482269383.

Vardoulakis, Ioannis (2019). *Cosserat Continuum Mechanics*. Ed. by E. Gerolymatou et al. Vol. 87. ISBN: 978-3-319-95155-3. DOI: 10.1007/978-3-319-95156-0. URL: http://link.springer.com/10.1007/978-3-319-95156-0.

Veveakis, E., S. Alevizos and I. Vardoulakis (2010). "Chemical Reaction Capping of Thermal Instabilities during Shear of Frictional Faults". In: *Journal of the Mechanics and Physics of Solids* 58.9, pp. 1175–1194. ISSN: 00225096. DOI: 10.1016/j.jmps.2010.06.010.

Veveakis, E., I. Stefanou and J. Sulem (May 2013). "Failure in Shear Bands for Granular Materials: Thermo-Hydro-Chemo-Mechanical Effects". In: *Géotechnique Letters* 3.2, pp. 31–36. ISSN: 2045-2543. DOI: 10.1680/geolett.12.00063.

Viswanath, P. and A. Das (2019). "Modelling the Response of Chemically Degraded Carbonate Sands". In: *Geomechanics and Geoengineering* 14.4, pp. 245–261. ISSN: 17486033. DOI: 10.1080/17486025.2019.1587178.

Wang, Z. and L.H. Poh (2018). "A Homogenized Localizing Gradient Damage Model with Micro Inertia Effect". In: *Journal of the Mechanics and Physics of Solids* 116, pp. 370–390. ISSN: 00225096. DOI: 10.1016/j.jmps.2018.04.007.

Wibberley, C.A.J. and T. Shimamoto (Jan. 2003). "Internal Structure and Permeability of Major Strike-Slip Fault Zones: The Median Tectonic Line in Mie Prefecture, Southwest Japan". In: *Journal of Structural Geology* 25.1, pp. 59–78. ISSN: 01918141. DOI: 10.1016/S0191-8141(02)00014-7.

Wichtmann, T. (2016). "Soil Behaviour under Cyclic Loading - Experimental Observations, Constitutive Description and Applications". Habilitation Thesis. Karlsruhe, Germany: Karlsruhe Insitute of Technology.

Wu, H. et al. (2019). "Compaction Bands in Tuffeau de Maastricht: Insights from X-ray Tomography and Multiscale Modeling". In: *Acta Geotechnica* 15.1, pp. 39–55. ISSN: 18611133. DOI: 10.1007/s11440-019-00904-9. URL: https://doi.org/10.1007/s11440-019-00904-9.

Zervos, A., P.C. Papanastasiou and I. Vardoulakis (2001). "Modelling of Localisation and Scale Effect in Thick-Walled Cylinders with Gradient Elastoplasticity". In: *International Journal of Solids and Structures* 38.30-31, pp. 5081–5095. ISSN: 00207683. DOI: 10.1016/S0020-7683(00)00337-1.

Zhang, Y. and G. Buscarnera (2017). "A Rate-Dependent Breakage Model Based on the Kinetics of Crack Growth at the Grain Scale". In: *Géotechnique* 67.11, pp. 953–967. ISSN: 0016-8505. DOI: 10.1680/jgeot.16.p.181.

— (2018). "Breakage Mechanics for Granular Materials in Surface-Reactive Environments". In: *Journal of the Mechanics and Physics of Solids* 112, pp. 89–108. ISSN: 00225096. DOI: 10.1016/j.jmps.2017.11.008.